



**HAL**  
open science

## Identification of distinct pathological signatures induced by patient-derived $\alpha$ -synuclein structures in nonhuman primates

Mathieu Bourdenx, Aurélien Nioche, Sandra Dovero, Marie-Laure Arotcarena, Sandrine M. J. Camus, Gregory Porras, Marie-Laure Thiolat, Nicolas P. Rougier, Alice Prigent, Philippe Aubert, et al.

### ► To cite this version:

Mathieu Bourdenx, Aurélien Nioche, Sandra Dovero, Marie-Laure Arotcarena, Sandrine M. J. Camus, et al.. Identification of distinct pathological signatures induced by patient-derived  $\alpha$ -synuclein structures in nonhuman primates. *Science Advances*, 2020, 6 (20), pp.eaaz9165. 10.1126/sciadv.aaz9165. hal-02611441v2

HAL Id: hal-02611441

<https://inria.hal.science/hal-02611441v2>

Submitted on 1 Feb 2025

**HAL** is a multi-disciplinary open access archive for the deposit and dissemination of scientific research documents, whether they are published or not. The documents may come from teaching and research institutions in France or abroad, or from public or private research centers.

L'archive ouverte pluridisciplinaire **HAL**, est destinée au dépôt et à la diffusion de documents scientifiques de niveau recherche, publiés ou non, émanant des établissements d'enseignement et de recherche français ou étrangers, des laboratoires publics ou privés.



Distributed under a Creative Commons Attribution - NonCommercial 4.0 International License

## NEUROSCIENCE

# Identification of distinct pathological signatures induced by patient-derived $\alpha$ -synuclein structures in nonhuman primates

M. Bourdenx<sup>1,2,\*†</sup>, A. Nioche<sup>1,2,3,4,\*‡</sup>, S. Dovero<sup>1,2,\*</sup>, M.-L. Arotcarena<sup>1,2,\*</sup>, S. Camus<sup>1,2</sup>, G. Porras<sup>1,2</sup>, M.-L. Thiolat<sup>1,2</sup>, N. P. Rougier<sup>1,2,5</sup>, A. Prigent<sup>6,7,8</sup>, P. Aubert<sup>6,7,8</sup>, S. Bohic<sup>9</sup>, C. Sandt<sup>10</sup>, F. Laferrière<sup>1,2</sup>, E. Doudnikoff<sup>1,2</sup>, N. Kruse<sup>11,12</sup>, B. Mollenhauer<sup>11,12</sup>, S. Novello<sup>13,14</sup>, M. Morari<sup>13,14</sup>, T. Leste-Lasserre<sup>15</sup>, I. Trigo Damas<sup>16,17</sup>, M. Goillandeau<sup>1,2</sup>, C. Perier<sup>17,18</sup>, C. Estrada<sup>19,20</sup>, N. Garcia-Carrillo<sup>21</sup>, A. Recasens<sup>17,18</sup>, N. N. Vaikath<sup>22</sup>, O. M. A. El-Agnaf<sup>22</sup>, M. T. Herrero<sup>19,20</sup>, P. Derkinderen<sup>6,7,8</sup>, M. Vila<sup>17,18,23,24</sup>, J. A. Obeso<sup>16,17</sup>, B. Dehay<sup>1,2§||</sup>, E. Bezard<sup>1,2§||</sup>

Copyright © 2020 The Authors, some rights reserved; exclusive licensee American Association for the Advancement of Science. No claim to original U.S. Government Works. Distributed under a Creative Commons Attribution NonCommercial License 4.0 (CC BY-NC).

Dopaminergic neuronal cell death, associated with intracellular  $\alpha$ -synuclein ( $\alpha$ -syn)-rich protein aggregates [termed “Lewy bodies” (LBs)], is a well-established characteristic of Parkinson’s disease (PD). Much evidence, accumulated from multiple experimental models, has suggested that  $\alpha$ -syn plays a role in PD pathogenesis, not only as a trigger of pathology but also as a mediator of disease progression through pathological spreading. Here, we have used a machine learning-based approach to identify unique signatures of neurodegeneration in monkeys induced by distinct  $\alpha$ -syn pathogenic structures derived from patients with PD. Unexpectedly, our results show that, in nonhuman primates, a small amount of singular  $\alpha$ -syn aggregates is as toxic as larger amyloid fibrils present in the LBs, thus reinforcing the need for preclinical research in this species. Furthermore, our results provide evidence supporting the true multifactorial nature of PD, as multiple causes can induce a similar outcome regarding dopaminergic neurodegeneration.

## INTRODUCTION

The seminal work of Braak and colleagues (1) suggesting that Lewy body (LB) pathology follows a predictable pattern of progression within the brain in Parkinson’s disease (PD) and the “host-to-graft” observation (2–4) led to the development of experimental models based on injection with  $\alpha$ -synuclein ( $\alpha$ -syn; the primary protein component of LB) assemblies (5). These experimental models suggest that  $\alpha$ -syn, in pathological conformations such as the one found in LBs, initiates a cascade of events leading to dopaminergic neuron degeneration and cell-to-cell propagation of  $\alpha$ -syn pathology through a self-templating mechanism.

Several studies have suggested that prefibrillar oligomers may represent one of the major neurotoxic entities in PD (6). This notion has been derived primarily from studies using large doses of recombinant  $\alpha$ -syn applied to cell cultures or injected in adult mice

overexpressing either mutant or wild-type  $\alpha$ -syn (7) and recently in macaque monkeys (8). In agreement with these findings, we have shown that intracerebral injection of low doses of  $\alpha$ -syn-containing LB extracts, purified from the substantia nigra pars compacta (SNpc) of postmortem PD brains, promotes  $\alpha$ -syn pathology and dopaminergic neurodegeneration in wild-type mice and nonhuman primates (9). This neuropathological effect was directly linked to the presence of  $\alpha$ -syn in LB extracts, since immunodepletion of  $\alpha$ -syn from the LB fractions prevented the development of pathology following injection into wild-type mice.

In this study, we aimed at characterizing this experimental model of synucleinopathy in nonhuman primates. The initial study design was to inject fractions derived from the same PD patients containing either soluble and small  $\alpha$ -syn aggregates (hereafter named nLB) or LB-type aggregates (hereafter named LB). However, because of

<sup>1</sup>Univ. de Bordeaux, Institut des Maladies Neurodégénératives, UMR 5293, F-33000 Bordeaux, France. <sup>2</sup>CNRS, Institut des Maladies Neurodégénératives, UMR 5293, F-33000 Bordeaux, France. <sup>3</sup>Institut Jean Nicod, Département d’études cognitives, ENS, EHESS, PSL Research University, 75005 Paris, France. <sup>4</sup>Institut Jean Nicod, Département d’études cognitives, CNRS, UMR 8129, Paris, France. <sup>5</sup>INRIA Bordeaux Sud-Ouest, 33405 Talence, France. <sup>6</sup>INSERM, U1235, Nantes F-44035, France. <sup>7</sup>Nantes University, Nantes F-44035, France. <sup>8</sup>CHU Nantes, Department of Neurology, Nantes F-44093, France. <sup>9</sup>EA-7442 Rayonnement Synchrotron et Recherche Médicale, RSRM, University of Grenoble Alpes, 38000 Grenoble, France. <sup>10</sup>SMIS beamline, Synchrotron SOLEIL, l’orme des merisiers, 91192 Gif sur Yvette, France. <sup>11</sup>Paracelsus-Elena-Klinik, Kassel, Germany. <sup>12</sup>University Medical Center Goettingen, Institute of Neuropathology, Goettingen, Germany. <sup>13</sup>Department of Medical Sciences, Section of Pharmacology, University of Ferrara, via Fossato di Mortara 17-19, 44121 Ferrara, Italy. <sup>14</sup>Neuroscience Center and National Institute of Neuroscience, University of Ferrara, via Fossato di Mortara 17-19, 44121 Ferrara, Italy. <sup>15</sup>INSERM, Neurocentre Magendie, U1215, Physiopathologie de la Plasticité Neuronale, F-33000 Bordeaux, France. <sup>16</sup>HM CINAC, HM Puerta del Sur and CEU-San Pablo University Madrid, E-28938 Mostoles, Spain. <sup>17</sup>Center for Networked Biomedical Research on Neurodegenerative Diseases (CIBERNED), Instituto Carlos III, Madrid, Spain. <sup>18</sup>Neurodegenerative Diseases Research Group, Vall d’Hebron Research Institute (VHIR)–Center for Networked Biomedical Research on Neurodegenerative Diseases (CIBERNED), Barcelona, Spain. <sup>19</sup>Clinical and Experimental Neuroscience Unit, School of Medicine, Biomedical Research Institute of Murcia (IMIB), University of Murcia, Campus Mare Nostrum, 30100 Murcia, Spain. <sup>20</sup>Institute of Research on Aging (IUJE), School of Medicine, University of Murcia, 30100 Murcia, Spain. <sup>21</sup>Centro Experimental en Investigaciones Biomédica (CEIB), Universidad de Murcia, Murcia, Spain. <sup>22</sup>Neurological Disorders Research Center, Qatar Biomedical Research Institute (QBRI), Hamad Bin Khalifa University (HBKU), Education City, Qatar. <sup>23</sup>Department of Biochemistry and Molecular Biology, Autonomous University of Barcelona (UAB), Barcelona, Spain. <sup>24</sup>Catalan Institution for Research and Advanced Studies (ICREA), Barcelona, Spain.

\*These authors contributed equally to this work.

†Present address: Albert Einstein College of Medicine, Department of Developmental and Molecular Biology, 1300 Morris Park Ave., Bronx, NY 10461, USA.

‡Present address: Aalto University, School of Electrical Engineering, Department of Communications and Networking, 02150 Espoo, Finland.

§Corresponding author. Email: benjamin.dehay@u-bordeaux.fr (B.D.); erwan.bezard@u-bordeaux.fr (E.B.)

||These authors contributed equally to this work as co-last authors.

the unexpected finding that nonhuman primates, unlike mice, are susceptible to soluble or finely granular  $\alpha$ -syn, we sought to elucidate the response characteristics induced by either LB or noLB fractions. To achieve a thorough analysis of these  $\alpha$ -syn-related characteristics, we took advantage of the strength of machine learning algorithms for finding fine patterns among complex sets of data and developed a new method compatible with the constraints of experimental biology. Here, we report on the identification of primate-specific responses to selected  $\alpha$ -syn assemblies and their accompanying species-specific pathogenic mechanisms. Overall, our results support the concept of the multifactorial nature of synucleinopathies.

## RESULTS

### Purification and characterization of $\alpha$ -syn extracts from patients with PD

noLB and LB fractions were obtained from the SNpc of five sporadic PD brains exhibiting conspicuous LB pathology. The samples were processed through differential ultracentrifugation in a sucrose gradient and analyzed for the presence of  $\alpha$ -syn aggregates by filter retardation assay (Fig. 1A) (9). Further characterization of noLB and LB fractions was performed by colocalization of  $\alpha$ -syn and the amyloid dye Thioflavin S (Fig. 1B) as well as ultrastructural examination by electron microscopy (Fig. 1C). These assays confirmed the presence of misfolded  $\alpha$ -syn in both fractions. We also performed biochemical characterization of the stability of assemblies after proteinase K digestion (Fig. 1D) and detergent treatments (Fig. 1E), followed by  $\alpha$ -syn dot-blot assays. While total  $\alpha$ -syn content was comparable between selected fractions [as measured by  $\alpha$ -syn enzyme-linked immunosorbent assay (ELISA)], LB fractions showed higher resistance to proteinase K treatment (noLB  $t_{1/2} = 15.23$  min versus LB  $t_{1/2} > 60$  min) (Fig. 1D) and greater resistance to multiple detergents, including 8 M urea (Fig. 1E). We then measured the content of  $\alpha$ -syn aggregates using human  $\alpha$ -syn aggregation time-resolved Förster's resonance energy transfer (TR-FRET)-based immunoassay, which revealed a significantly higher amount of aggregated  $\alpha$ -syn in LB fractions (Fig. 1F). To obtain insight into the content of monomeric and aggregated  $\alpha$ -syn within noLB and LB fractions of patients with PD, we applied sarkosyl treatment to both fractions to induce physical separation and then performed velocity sedimentation and density floatation gradients to quantify these two populations and determine their relative abundance in each fraction (fig. S1, A to H). Notably, while LB fractions contained ~90% of aggregated  $\alpha$ -syn, noLB fractions were composed of ~10% of this pathological form of the protein (fig. S1I). In addition, to confirm the quality of the LB extraction, we performed a filter retardation assay, which showed that LB, but not noLB, fractions were highly enriched in known components of LBs, such as phosphorylated S129  $\alpha$ -syn, ubiquitin, p62, hyperphosphorylated tau, and  $\beta$ -amyloid (A $\beta$ ) (fig. S2A).

Micro-infrared spectroscopy of LB and noLB fractions was performed to show conformational changes in amyloid structures at the molecular level (fig. S2, B to E), and this confirmed the presence of  $\beta$  sheet structures in both assemblies (fig. S2, B and C). Although their velocity of sedimentation and density floatation characteristics were similar, the aggregates present in the LB and noLB fractions were different in nature on the basis of the evidence of micro-infrared spectroscopy. Principal components analysis (PCA) showed that, in LB fractions, large aggregates corresponding to the major pieces of LB were present (fig. S2D, cluster on the right). PCA further showed

that, in the range of 1590 to 1700  $\text{cm}^{-1}$ , the LB group contained a fraction of amyloid aggregates with different amyloid structures from those in the noLB group, as PCA clearly segregated them in two clusters (fig. S2, D and E). Together, these results suggest that while LB fractions primarily contained large aggregated  $\alpha$ -syn fibrils, noLB fractions contained soluble  $\alpha$ -syn and a smaller enrichment of  $\alpha$ -syn aggregates featuring a specific amyloid structure not found in LB fractions.

Data from several studies suggest that both recombinant  $\alpha$ -syn preformed fibrils (10, 11) and patient-derived  $\alpha$ -syn (9) can promote pathogenic templating of endogenous  $\alpha$ -syn, ultimately leading to dopaminergic neurodegeneration in SNpc. The  $\alpha$ -syn content quantified by ELISA, as previously reported, was (9) noLB (41.33  $\mu\text{g}/\mu\text{l}$ ) and LB (24.52  $\mu\text{g}/\mu\text{l}$ ). To allow comparison between experimental groups, we diluted both pools of fractions to the least concentrated pool (24  $\mu\text{g}/\mu\text{l}$ ). Then, those fractions were tested for their pathogenic effects on tyrosine hydroxylase (TH)-positive dopaminergic neurons in primary mesencephalic cultures (fig. S3A) and in wild-type mice. Four months after supranigral injection, LB-injected mice displayed, as expected, significant dopaminergic degeneration, while noLB-injected mice showed no dopamine neuron loss (Fig. 1, G and H). This confirms previously reported toxicity of other SNpc-derived LB fractions (9), validating the toxicity of the preparation to further injection into nonhuman primates.

### Intrastratial injection of LB and noLB fractions from patients with PD induces nigrostriatal neurodegeneration in baboon monkeys

To determine the mechanisms of  $\alpha$ -syn aggregate toxicity in a species closer to humans, adult baboon monkeys ( $n = 4$  to 7 per experimental group) received bilateral stereotactic injections (100  $\mu\text{l}$ ) of either LB or noLB fractions into the putamen. Since our previous studies indicated that ongoing pathogenic effects can already be measured at 14 months after LB injection, we decided to further extend this time frame to 24 months in the attempt to potentially observe disease-relevant lesions. Two years after administration, LB-injected monkeys displayed significant striatal dopaminergic terminal loss both in the putamen and in the caudate nucleus, which was accompanied by a significant decrease in TH immunoreactivity in the SNpc (Fig. 2). Stereological counts showed that LB-injected animals exhibited TH- and Nissl-positive cell loss in the SNpc (16 and 23%, respectively; control animals,  $176,719 \pm 13,110$  TH-positive neurons; LB-injected animals,  $139,104 \pm 13,256$  TH-positive neurons; noLB-injected animals,  $138,046 \pm 16,615$  TH-positive neurons). No overt parkinsonism was observed, however, since the extent of the lesion remained below the threshold for motor symptom appearance, i.e., 45% of cell loss (12). However, using a validated ethological evaluation, we were able to unravel changes in the behavioral profiles characterized by a decrease in spontaneous locomotion associated with social isolation, following LB and noLB injections (fig. S4). These two phenotypes could be reminiscent of early parkinsonism, notably the loss of interest for reinforcing situation (i.e., social interaction), and compatible with the level of nigrostriatal neurodegeneration following LB and noLB injections.

At odds with mice either generated for the purpose of this study (Fig. 1, G and H) and previously characterized (9) or produced in the context of other in-house studies, noLB-injected monkeys showed degeneration of the nigrostriatal pathway including dopaminergic cell loss (i.e., 16% of TH-positive neurons and 28% of Nissl-positive neurons quantified by stereology), similar to that observed in

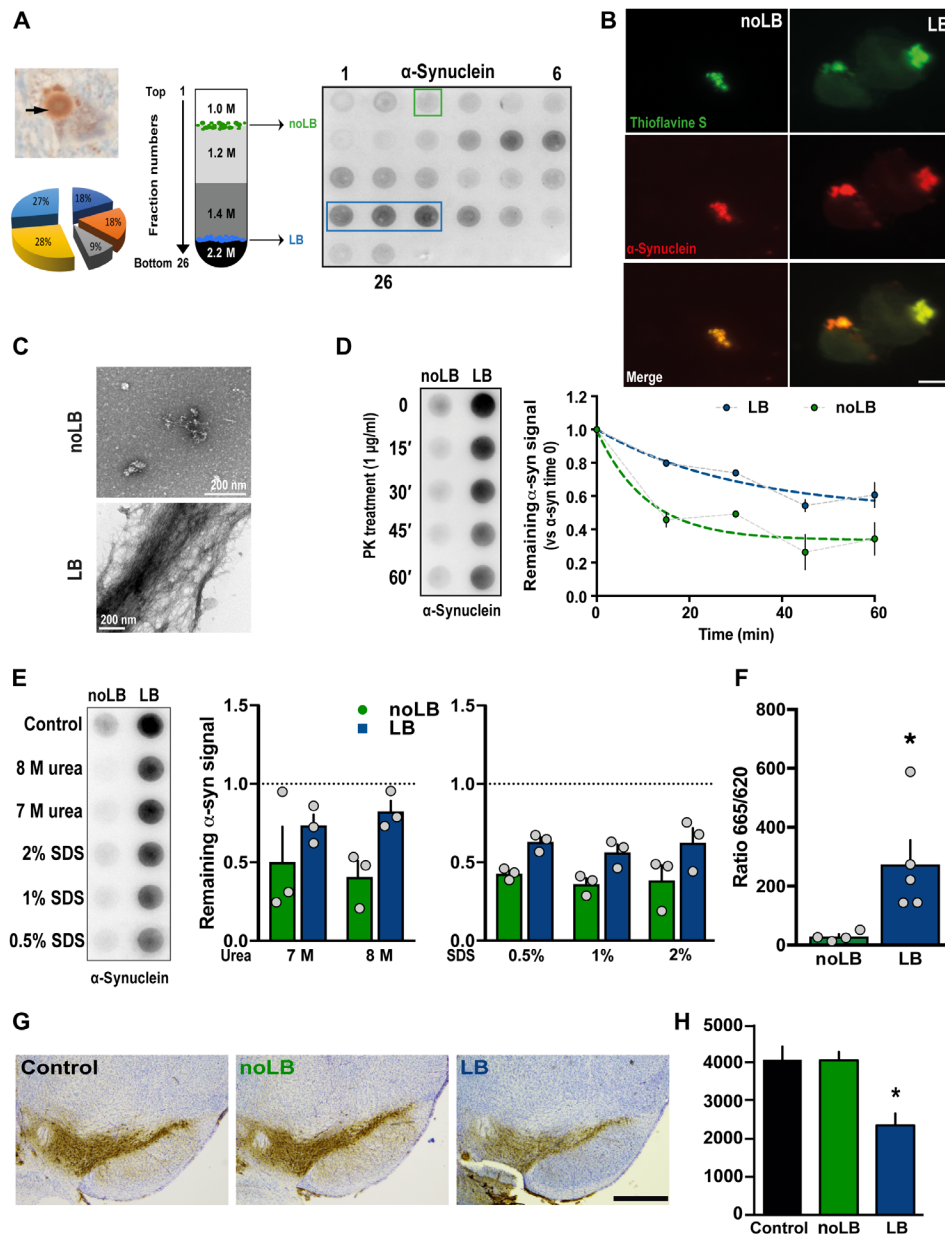


**Fig. 1. Purification and characterization of LBs and noLB inocula from PD brains.** (A) Left: Immunohistochemistry image of  $\alpha$ -syn–positive LB (arrows) in nigral postmortem brain samples (PD #1;  $\alpha$ -syn in brown and neuromelanin in dark brown) before sucrose gradient purification. The pie chart indicates the relative contribution of the five patients to the final pool of LB and noLB inocula. Middle: Schematic representation of the sucrose gradient fractionation procedure used to purify LB/noLB-containing fractions from freshly frozen postmortem nigral brain tissue of five sporadic patients with PD. Right: Filter retardation assay probed with a human  $\alpha$ -syn antibody to assess the presence of  $\alpha$ -syn aggregates in the different fractions obtained by sucrose gradient fractionation from freshly frozen postmortem nigral brain tissue from sporadic patients with PD (PD #1). Green square indicates noLB-containing fraction, and blue rectangle highlights LB-containing fraction selected to prepare the mixture used for injections. (B) Confocal examination of purified noLB and LB fractions with  $\alpha$ -syn immunofluorescence (red) and thioflavin S (green) staining. Both LB and noLB present thioflavin S–positive aggregates but much smaller in noLB fractions. Scale bar, 10  $\mu$ m. (C) Ultrastructural examination of noLB and LB fractions by electron microscopy showing massive fibrils in LB fractions, while noLB fractions contain, besides soluble  $\alpha$ -syn, some punctiform small-size aggregates. (D) noLB and LB fractions derived from PD brains (left) were treated with proteinase K (PK) (1  $\mu$ g/ml) for 0, 15, 30, 45, and 60 min and analyzed by immunoblotting with syn211 antibody. The median effective concentration ( $EC_{50}$ ) value was determined as the concentration at which this ratio is decreased by 50%. The corresponding  $EC_{50}$  value for LB (>60 min) was approximately fourfold greater than with noLB (15.23 min). (E) noLB and LB fractions were treated for 6 hours with increasing concentrations of either urea or SDS or buffer as control. Syn211 was used to detect the forms of  $\alpha$ -syn. The LB fractions appear to be more resistant to breakdown compared with noLB fractions in both urea ( $F_{1,8} = 6.063, P = 0.0392$ ) and SDS treatments ( $F_{1,12} = 17.41, P = 0.0013$ ). The dotted lines show levels of control fractions. Comparison was made using two-way analysis of variance (ANOVA). (F) TR-FRET immunoassay analysis of noLB and LB fractions. Fluorescence measurements were taken 20 hours after antibody. Analysis by unpaired Student's *t* test ( $t_7 = 2623, P = 0.0343$ ). \* $P < 0.05$ . Means  $\pm$  SEM,  $n = 4$  to 5. (G) Representative pictures of tyrosine hydroxylase (TH)–positive SNpc neurons (brown; Nissl staining in purple) in noninjected and noLB- or LB-injected mice at 4 months after injections. Scale bar, 500  $\mu$ m. (H) Quantification of TH-positive SNpc neurons by stereology in control and LB- and noLB-injected mice. Control mice,  $n = 10$ ; LB-injected mice at 4 months,  $n = 10$ ; noLB-injected mice at 4 months,  $n = 10$ . Comparison was made using one-way ANOVA followed by Tukey test for multiple comparisons. \* $P < 0.05$  compared with control and noLB-injected mice at 4 months.



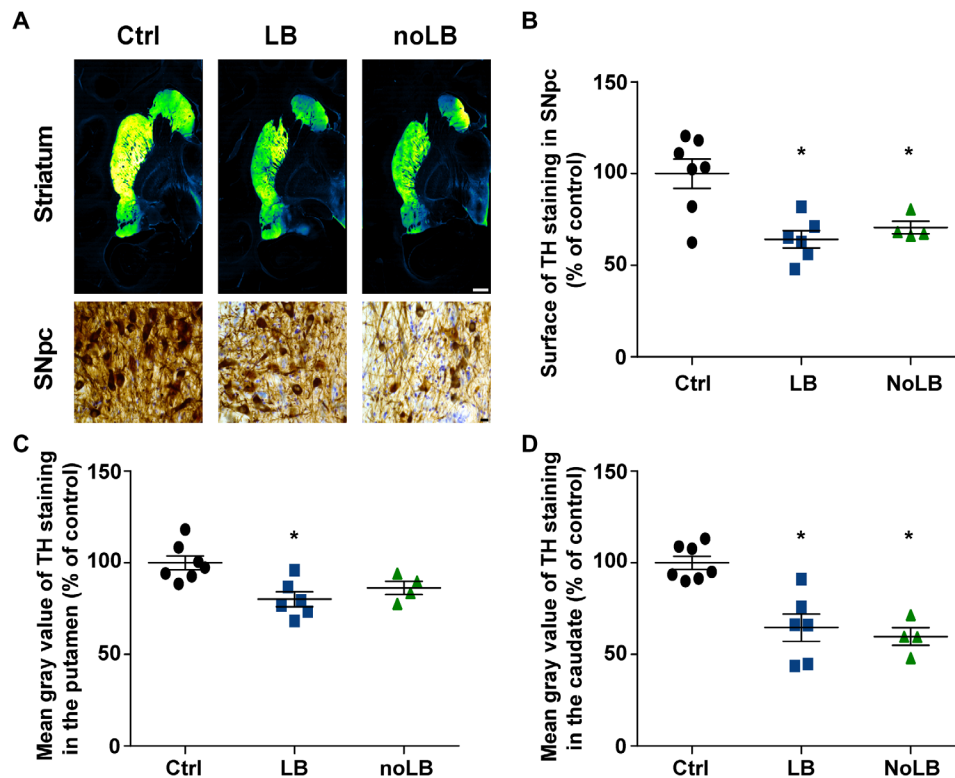


**Fig. 2. Intrastratial injection of LB and noLB fractions from patients with PD induces nigrostriatal neurodegeneration in baboon monkeys.** (A) TH staining at striatum and SNpc levels. A green fire blue LUT (lookup table) was used to enhance contrast and highlight the difference between noninjected and LB- and noLB-injected baboon monkeys at the striatum level. Scale bars: 5 mm (striatum) and 10  $\mu$ m (SNpc). (B) Scatter plot of TH immunostaining in SNpc ( $F_{2,14} = 9.439$ ,  $P = 0.0025$ ; control versus LB-injected,  $P = 0.0029$ ; control versus noLB-injected,  $P = 0.0248$ ). (C and D) Scatter plots of mean gray values of striatal TH immunoreactivity in the putamen ( $F_{2,14} = 7.313$ ,  $P = 0.0067$ ; control versus LB-injected,  $P = 0.0059$ ) (C) and in the caudate ( $F_{2,14} = 16.25$ ,  $P = 0.0002$ ; control versus LB-injected,  $P = 0.0008$ ; control versus noLB-injected,  $P = 0.0008$ ) (D) in noninjected and LB- and noLB-injected baboon monkeys. The horizontal line indicates the average value per group  $\pm$  SEM ( $n = 7$  from control animals;  $n = 6$  for LB-injected animals;  $n = 4$  for noLB-injected animals). Comparison was made using one-way ANOVA and Tukey's correction for multiple comparisons. \* $P < 0.05$  compared with control animals.

LB-injected monkeys (Fig. 2). Facing such an unexpected finding, we aimed to identify specific characteristics of the pathological mechanisms involved in  $\alpha$ -syn toxicity induced by each fraction independently using a large-scale approach in combination with machine learning for pattern identification.

### Machine learning algorithm predicts nigrostriatal degeneration

We performed an exploratory approach and aimed to distinguish relevant variables allowing accurate prediction of neurodegeneration (i.e., to operate a feature selection). Overall, we investigated a large number of variables tapping on behavioral, histological, biochemical, transcriptional, and biophysical approaches (Fig. 3A) applied to several brain areas ( $n = 40$ ; Fig. 3B), totalizing 180 variables measured for each individual (fig. S5A for variable abbreviation nomenclature, table S1 for exhaustive list of variables, and table S2 for all raw data). We first extracted from this dataset every variable that actually quantified neurodegeneration (i.e., dopaminergic markers such as TH or dopamine transporter evaluated by immunohistochemistry), ending up with 163 variables per animal.

Then, to operate feature selection, we designed a distributed algorithm using multiple-layer perceptron (MLP) (13), a classic machine learning algorithm based on artificial neural network that

is able to approximate virtually any functions (14). This algorithm was given, as input, the data obtained for each animal for the 163 aforementioned variables, and its output is a rank of these variables regarding their ability to predict three indicators of dopaminergic tract integrity, which were levels of TH staining in (i) the SNpc, (ii) the putamen, and (iii) the caudate nucleus.

The main difficulty was to overcome the large number of input variables (163) compared to the sample size ( $n = 4$  to 7 per group), which can induce a selection and reporting bias (15). To tackle this “ $p > n$ ” problem, instead of using a single network that could be prone to overfitting, we put in competition several networks.

Each MLP was composed of a single hidden layer of three neurons (Fig. 3C). It has as input a subset of three variables (of the 163) and as output the three indicators of dopaminergic tract integrity. In total, we used 708,561 sets of three input variables. Every instance of MLP was trained with 80% of our sample (always a combination of control and injected animals) and tested on the remaining 20%. The performance of each set of three input variables was evaluated according to the difference between the predicted values of TH staining and the actual ones.

We focused on the top 1% of the best networks and counted the occurrence of each of the 163 variables in the subset of three variables used by these best networks (Fig. 3C). We ranked each variable

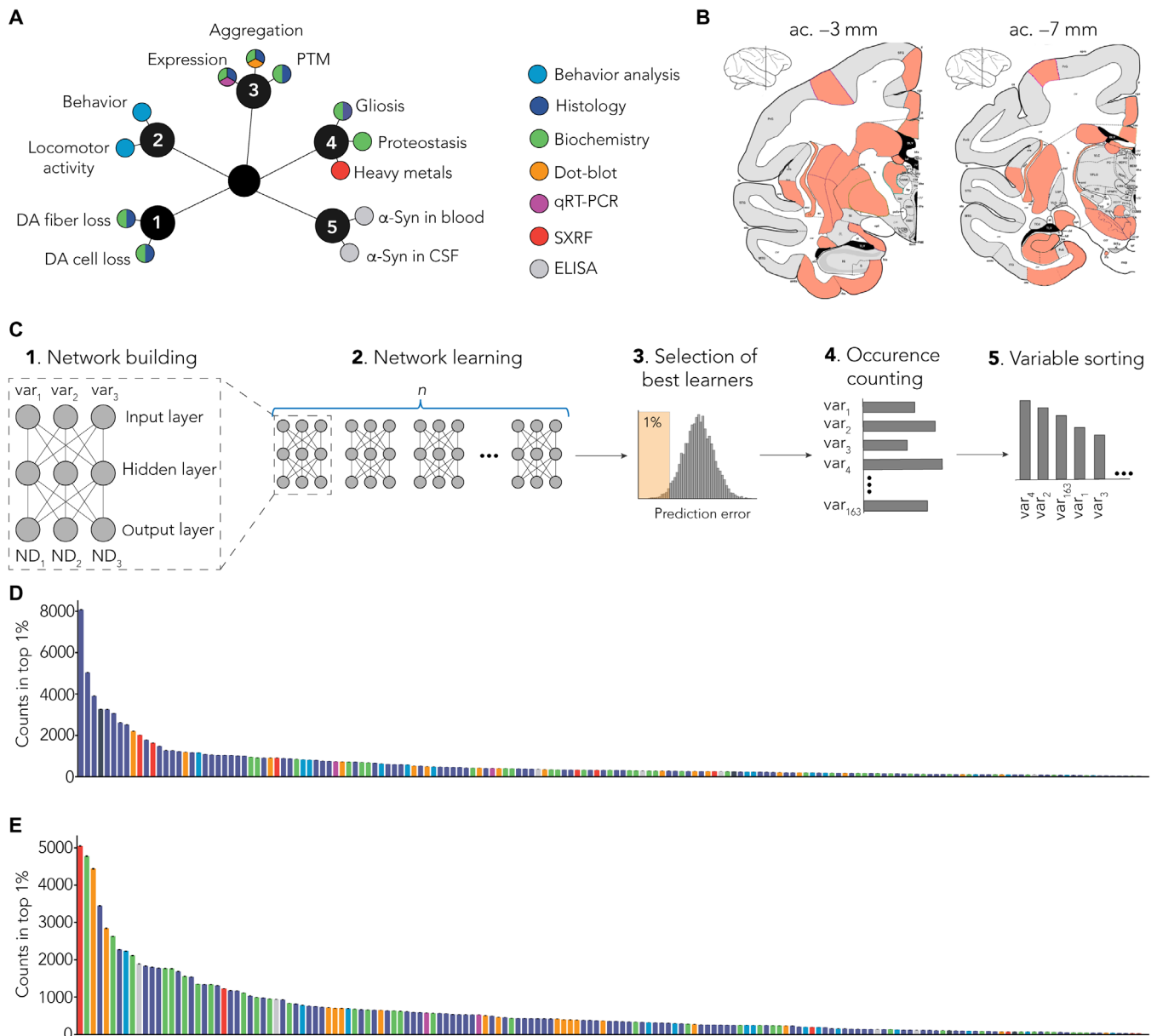


**Fig. 3. MLP-based identification of specific signature.** (A) Several end points ( $n = 180$ ) were measured using multiple methods (colors). End points can be grouped as clusters: (1) dopaminergic degeneration, (2) behavior, (3)  $\alpha$ -syn-related pathology, (4) non- $\alpha$ -syn-related pathology, and (5) putative biomarkers. PTM, posttranslational modification; CSF, cerebrospinal fluid; qRT-PCR, quantitative reverse transcription polymerase chain reaction; DA, dopamine. (B) Multiple brain regions ( $n = 40$ ) were investigated from coronal sections at two levels: anterior commissure (ac.),  $-3$  mm (striatum and entorhinal cortex) and  $-7$  mm (SNpc and hippocampus). SXRF, nano-synchrotron X-Ray fluorescence. (C) Detailed methodology. (1) Representative scheme of one MLP predicting three neurodegeneration-related variables ( $ND_1$ ,  $ND_2$ , and  $ND_3$ ) with three experimental variables as input ( $var_1$ ,  $var_2$ , and  $var_3$ ). Of the 180 variables measured in total, 163 were used as inputs for the MLP. (2) One MLP was trained for every unique combination of three variables. (3) Combinations were ranked on the basis their prediction error, and top 1% was selected for further analysis. (4) Combinations were deconvoluted to extract single variables and count occurrence of individual variables. (5) Variables were sorted on the basis of the number of occurrences in the top 1% of the best combination. (D) Raw ranking obtained for LB-injected animals. Color code highlights measurement methods as in (A). (E) Raw ranking obtained for noLB-injected animals. Color code highlights measurement methods as in (A).

according to the number of occurrences (Fig. 3C) for LB-injected (Fig. 3D) and noLB-injected (Fig. 3E) animals independently.

To avoid possible overfitting, we used several methods in combination. First, we performed cross-validation by splitting the dataset into two parts: a training and a testing set of data. Eighty percent of the data were randomly selected to train the networks (and in-

dependently for each network), while the 20% remaining were used to evaluate the networks. Then, to evaluate the robustness of the quality of prediction for a given set, we repeated this cross-validation step 50 times for every set of three input variables (each network was trained and tested using a different partition of the dataset; total number of networks, 35,428,050). Last, we generated random data

and used them as input for the MLP. As expected, performances were significantly lower compared to our actual dataset (fig. S5, B and C).

Overall, this unique approach allowed us to rank input variables according to their explanatory power and therefore to extract the strongest predictors of neurodegeneration for each experimental group. Despite similar levels of nigrostriatal degeneration between LB- and noLB-injected animals (Fig. 2B), the algorithm allowed us to identify differential variable sorting patterns (Fig. 3, D and E).

### MLP-derived signatures can identify unique characteristics between experiment group

Next, we compared the LB and noLB characteristics using the rank-rank hypergeometric overlap (RRHO) test (Fig. 4A). Low similarity was observed for the highly ranked variables, suggesting specific differences in the biological response to the injection of LB or noLB (Fig. 4B). Focusing on the 20 first variables that showed low similarity between groups, we found that LB-exposed monkeys were characterized by both quantitative and qualitative changes in  $\alpha$ -syn levels (i.e., phosphorylation at Ser<sup>129</sup> and aggregation) especially in cortical areas corroborated by distinct methodologies and by a dysfunctional equilibrium in neurochemistry of basal ganglia output structures

classically associated with parkinsonism (Fig. 4C and fig. S6) (16). Conversely, noLB-exposed monkeys exhibited more diverse nigrostriatal-centric characteristics with variables related to  $\alpha$ -syn aggregation, proteostasis, and Zn homeostasis (Fig. 4D and fig. S7). Together, we identified specific properties for both groups with limited overlap (35%; 7 of 20 variables) for an identical level of degeneration.

### Retrospective literature search validates MLP-derived signatures

We next used a retrospective analysis to validate the relevance of the MLP-derived signature in PD. Although some variables have never been investigated in the context of PD, others have been studied, and reports exist in the literature. For instance, the amount of phosphorylated Ser<sup>129</sup>  $\alpha$ -syn in the entorhinal (h.psyn.ctx.er.ant) and parahippocampal (h.psyn.ctx.phipp) cortex—first and second best predictors for the LB group—has been already associated with PD pathology. Studies of postmortem brains from patients with PD revealed the presence of LB in these regions, which was correlated with disease progression (17), and predicted cognitive deficit in patients with PD (18). The anterior entorhinal cortex has also been shown to be affected by severe  $\alpha$ -syn pathology, related to olfactory

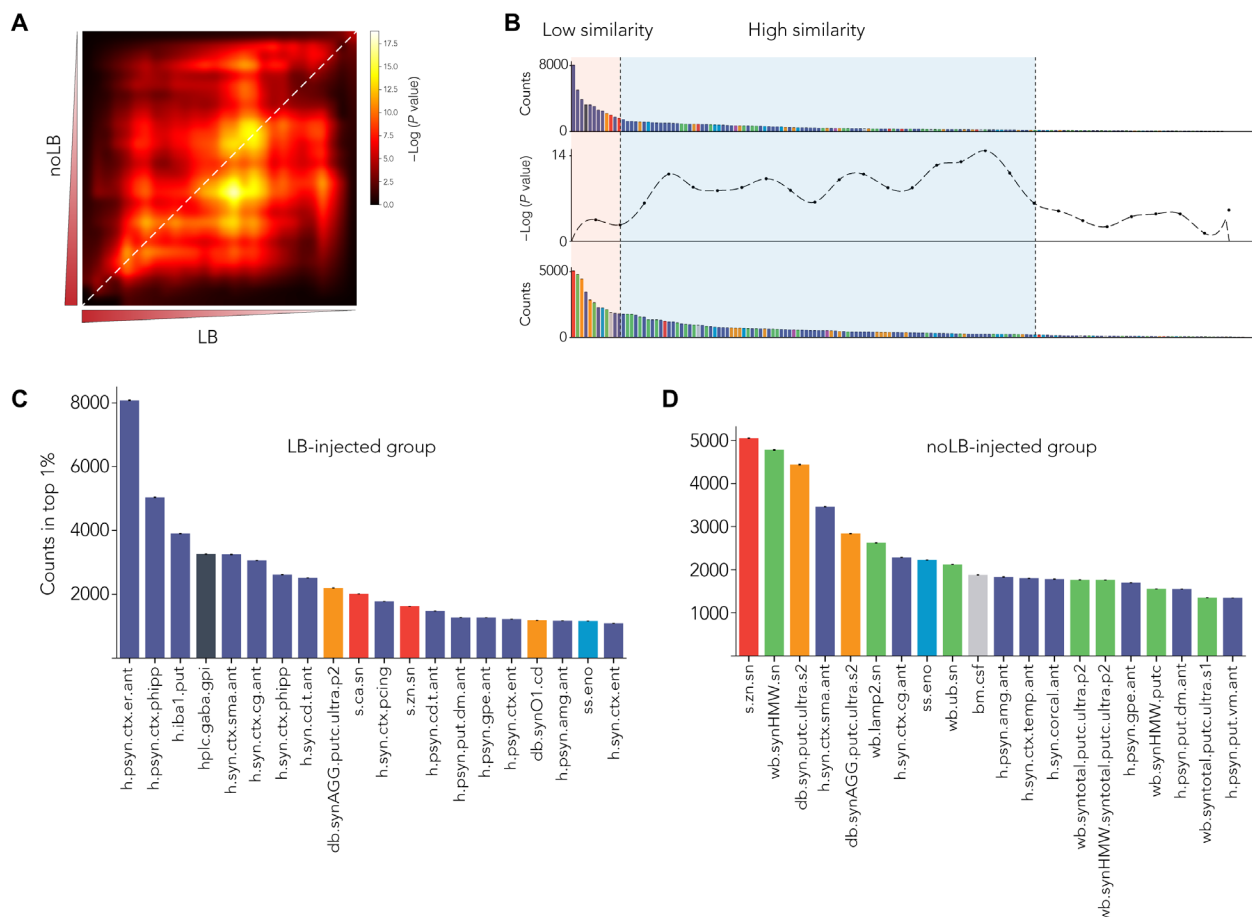


**Fig. 4. Direct comparison of MLP-derived signatures shows specific pattern between experiment groups.** (A) RRHO test between variable sorting of LB- and noLB-injected animals. Highly enriched variables are in the lower left corner. Diagonal (highlighted by white dashed line) was extracted to do a bin-to-bin comparison between LB and noLB signatures. (B) Signatures were aligned with RRHO and show low similarity in highly enriched variables (light orange background) and higher similarity for lower rank variables (pale blue background). (C and D) First 20 enriched variables for both LB-injected animals (C) and noLB-injected animals (D). Color code is similar to Fig. 2A. Detailed of variable names can be found in table S1. Bars are means  $\pm$  99% confidence interval estimated by bootstrap.

dysfunction in prodromal phases of PD pathology (19). In addition, increased levels of phosphorylated Ser<sup>129</sup>  $\alpha$ -syn in sensorimotor (h.syn.ctx.sma.ant) and cingulate cortices (h.syn.ctx.cg.ant), shared by both LB and noLB signatures, have already been reported by our group in an independent cohort of nonhuman primates (9).

LB and, especially, noLB signatures showed that variables related to  $\alpha$ -syn aggregation status were among the best predictors (LB, one in top 10 best predictors; noLB, three in top 10 best predictors): aggregated  $\alpha$ -syn in the putamen measured by filter retardation assay (db.syn.AGG.putc.ultra.p2 and db.syn.putc.ultra.s2) and high-molecular weight  $\alpha$ -syn in the SN (wb.syn.HMW.sn). This was highly expected from the literature as  $\alpha$ -syn aggregation has been associated with PD pathology (20).

Variables related to the proteostasis network (levels of the lysosomal receptor LAMP2—wb.lamp2.sn—sixth or amount of ubiquitinated proteins—wb.ub.sn—ninth) were more specifically associated with the noLB signature. This is of high interest as proteostasis defect is more and more considered as a key step in pathogenicity (21, 22).

Levels of the microglia marker, ionized calcium-binding adapter molecule 1 (Iba1), was ranked as the third best predictor of neurodegeneration in the LB signature. Microglial inflammatory response was shown to be implicated in neurodegeneration in many animal models, including  $\alpha$ -syn overexpressing and toxin-based animal model of PD (23).

Last, postmortem analysis of Zn<sup>2+</sup> concentration in the brains of patients with PD has shown elevated levels in the striatum and SNpc (24), and a recent meta-analysis showed a decrease in circulating Zn<sup>2+</sup> levels in patients with PD (25). In experimental models of PD, Zn<sup>2+</sup> accumulation has been associated with dopaminergic degeneration in rodent exposed to mitochondrial toxins (26).

### Experimental confirmation of MLPs' prediction

We aimed to confirm the relevance of the top first MLP selected variables. Because the LB signature was associated with changes in  $\alpha$ -syn phosphorylation in cortical areas, we analyzed side by side the levels of  $\alpha$ -syn and phosphorylated Ser<sup>129</sup>  $\alpha$ -syn in 18 brain regions (Fig. 5A). In agreement with the LB signature obtained from the MLP, LB-injected monkeys displayed a stronger accumulation of phosphorylated Ser<sup>129</sup>  $\alpha$ -syn compared to noLB-injected animals (Fig. 5, A and B). In addition, the two most enriched variables of the LB signature [i.e., phosphorylated  $\alpha$ -syn levels in parahippocampal and entorhinal cortices (Fig. 4C)] showed significant negative correlations with degrees of degeneration (Fig. 5, C and D), thus confirming their ability to predict neurodegeneration.

Then, we decided to confirm the relevance of one of the strongest predictors, the levels of Zn<sup>2+</sup> in the SNpc in independent experiments. First, we observed a significant increase in Zn<sup>2+</sup> in noLB-injected mice compared to sham- or LB-injected mice (fig. S8A). Second, we analyzed the levels of Zn<sup>2+</sup> in LB-injected macaque monkeys from a previous study of our laboratory (9). Despite the fact that these experiments were performed in a different nonhuman primate subspecies, injection of LB in the putamen (similar to the present study) or above the SNpc (different from the present study) induced elevation of Zn<sup>2+</sup> levels in the SNpc, as measured by synchrotron radiation x-ray fluorescence (SR-XRF) (fig. S8B). Notably, the dimension of the effect was similar across studies (fig. S8E). Then, to understand whether that modulation Zn<sup>2+</sup> levels was specific to our experimental paradigm, we measured Zn<sup>2+</sup> levels in the context of adeno-associated virus-mediated overexpression of mutant human  $\alpha$ -syn in both rats

and marmoset monkeys (27) using the same methodology (fig. S8, C and D). Here, overexpression of  $\alpha$ -syn did not trigger accumulation of Zn<sup>2+</sup> in the SNpc [despite inducing dopaminergic neurodegeneration (27)], suggesting that this phenomenon is specific to seeding experiment paradigms. This assertion could be confirmed in other seeding-based models such as striatal preformed fibril injection (8, 10) or more refined models using specific types of fibrils or oligomers (28).

Last, we analyzed a publicly available cortical proteomic database of healthy individual and patients with PD. We observed that several Zn<sup>2+</sup> transporters were elevated in the brains of patients with PD, thus suggesting a zinc dyshomeostasis in patients (fig. S8F). Plasma membrane transporters such as the zinc transporter 1 (ZnT1), the Zrt-/Irt-like protein 6 (ZIP6), and the ZIP10 showed increased levels (fig. S8, G to I), while the synaptic vesicle membrane transporter ZnT3 remained constant (fig. S8J).

### Association metric shows independence of strong predictors

As we used combinations of three variables and because of the structure of MLPs, one could expect that some combinations would complement each other to allow finer prediction of neurodegeneration levels. To address this question, we used a classic measurement of association in the field of data mining: lift (29) and plotted the results as network plots showing association (edge size) and enrichment in the best learners (node size). Lift calculation was corrected for error prediction to avoid detrimental association between variables. The first observation was that the most enriched variables (top 3 to 5) appeared to be self-sufficient to predict the neurodegeneration levels with minimal error (Fig. 6). Some variables, with modest enrichment showed strong positive associations that were specific to each experimental group. Associated variables in LB-injected monkeys were (i)  $\alpha$ -syn-related parameters along the SNpc-striatum-cortex axis, an impairment of locomotion and the ethologically defined orientation of the animals toward their environment (Fig. 6, inset #1); and (ii) oligomeric  $\alpha$ -syn species measured in the midbrain and striatum equally associated, but to lesser extent, with  $\alpha$ -syn levels in cortex and plasma (Fig. 6, inset #2).

In noLB-injected animals, the analysis shed light upon the relative abundance of two members of the macroautophagy pathway (Fig. 6B, inset #3) and the balance between monomeric and high-molecular weight species of  $\alpha$ -syn in the putamen (Fig. 6B, inset #4). This disruption of the nigrostriatal pathway reverberated upon the basal ganglia physiology as  $\gamma$ -aminobutyric acid (GABA) levels in the internal globus pallidus, i.e., the basal ganglia output structure, were associated with a decreased social behavior (Fig. 6B, inset #5).

### DISCUSSION

In the present study, we report that injection of distinct  $\alpha$ -syn assemblies derived from patients with PD in nonhuman primates leads to dopaminergic degeneration through discrete mechanisms. Applying a machine learning method, we gained insight into unique signatures of degeneration induced by injection of two distinct  $\alpha$ -syn pathogenic assemblies (i.e., those contained in the LB and noLB fractions derived from idiopathic PD patients' brains). To do so, we built a large dataset with 180 variables obtained from behavioral, histological, biochemical, transcriptional, and biophysical approaches applied to several brain areas for each individual. By using a distributed MLP algorithm that we developed for the purpose of this study, we



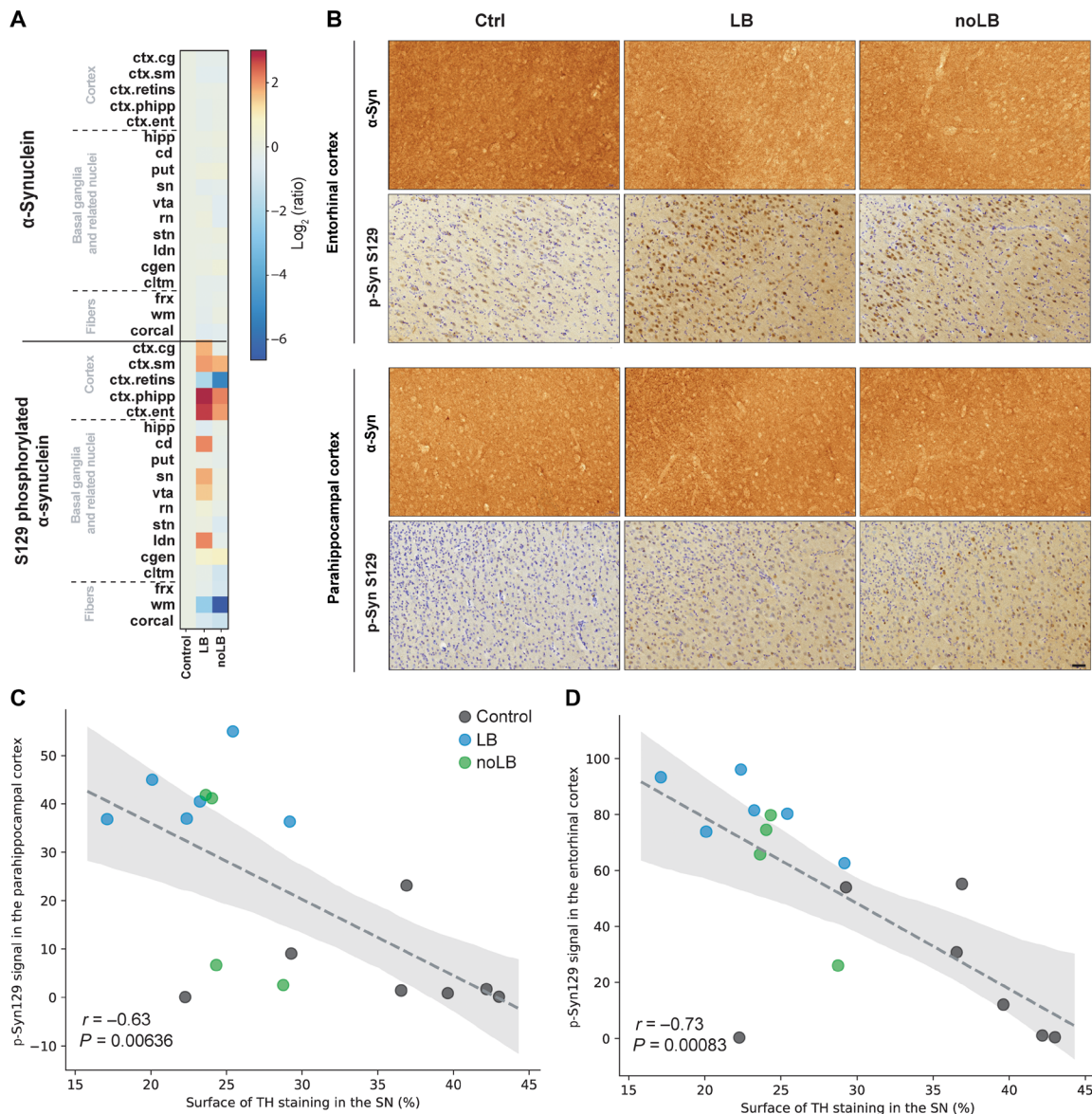


**Fig. 5. Levels of  $\alpha$ -syn and phosphorylated  $\alpha$ -syn in different brain regions.** (A) Heat map representing the surface of  $\alpha$ -syn and S129 phosphorylated  $\alpha$ -syn immunostaining intensity in the brain of noninoculated and LB- and noLB-inoculated baboon monkeys. The heat maps show all brain regions measured and are organized according in three main groups: cortical, basal ganglia, and subcortical areas. From top to bottom: cingulate cortex (ctx.cg), sensorimotor cortex (ctx.sm), retro-insular cortex (ctx.retins), parahippocampal cortex (ctx.phipp), entorhinal cortex (ctx.ent), hippocampus (hipp), caudate nucleus (cd), putamen (put), substantia nigra (sn), ventral tegmental area (vta), red nucleus (rn), subthalamic nucleus (stn), lateral dorsal nucleus (ldn), lateral geniculate nucleus (cgen), claustrum (cltm), fornix (frx), white matter (wm), and corpus callosum (corcal). The color bars represent the log<sub>2</sub> value of the ratio of each brain regions. (B) Representative pictures of  $\alpha$ -syn and phosphorylated  $\alpha$ -syn (p-Syn S129) staining in the entorhinal and parahippocampal cortices. (C and D) Correlation between levels of phosphorylated  $\alpha$ -syn in the parahippocampal cortex (C) and the entorhinal cortex (D) with levels of TH staining in the substantia nigra (SN). Dashed lines indicate the linear regression. Gray area indicates the 95% confidence interval around of the linear regression.

identified characteristics that give insight into the strongest predictors of neurodegeneration for each experimental group. We have therefore described that distinct  $\alpha$ -syn assemblies leading to similar degeneration in monkeys are associated with different mechanisms, hence experimentally confirming the true multifactorial nature of synucleinopathies.

Our results illustrate that both small oligomeric and larger  $\alpha$ -syn assemblies induce dopaminergic degeneration in nonhuman primates. This finding was unexpected, since previous mouse studies from

our laboratory showed that noLB injection did not have any observable impact on dopaminergic degeneration,  $\alpha$ -syn accumulation, or phosphorylation (9). In agreement, other groups also showed the absence of toxicity of soluble recombinant  $\alpha$ -syn in mice (10). One possible explanation is that primate dopaminergic neurons could be highly susceptible to  $\alpha$ -syn toxicity. This could be, in part, due to their unique cellular architecture (30), a feature already known to contribute to the selective vulnerability of these neurons in PD (31). The large and complex axonal arbor of dopamine neurons makes



different from the pool of three patients used in our previous study in mice (9). In mice experiment performed in this study (fig. S3B), we observed the same level of dopaminergic degeneration (~40% at 4 months after injection).

The unexpected observation that, in nonhuman primates, the noLB fraction is toxic to the same extent as the LB fraction suggests the existence of previously unrecognized forms of  $\alpha$ -syn toxicity. Several studies have suggested that prefibrillar oligomeric species are the toxic  $\alpha$ -syn species (6, 34). Our biochemical studies showed that noLB and LB fractions had different amyloid properties (Fig. 1), contents (figs. S1 and S2A), and structures (fig. S2, B to E). LB fractions contained mostly large aggregated  $\alpha$ -syn fibrils and some smaller aggregates, while noLB fractions contained a much lower amount (10-fold) of smaller aggregates and soluble  $\alpha$ -syn. The smaller aggregates in LB and noLB fractions were different in nature, as shown by micro-infrared spectroscopy (fig. S2, B to E). One could hypothesize that the observed effect is due to a species in common between LB and noLB. However, because of the extent of degeneration, which was similar between the two experimental groups, and the  $\alpha$ -syn content dissimilarities, both in terms of amount and nature, this appears very unlikely.

We cannot rule out, however, that other proteins contained in these fractions play a role. The question of factors contributing to the pathology when using patient-derived material is of utmost importance. We performed a filter retardation-based study to characterize if these proteins are enriched in our fractions. As reported in fig. S2A, tau and A $\beta$  are enriched in some LB fractions, which is expected as LBs are mature aggregates that have been shown to contain many proteins. In our previous paper (9), we used two approaches to ensuring that  $\alpha$ -syn was essential to the observed toxicity. First, we injected immunodepleted fractions and observed an absence of dopaminergic degeneration. Second, we injected fractions to  $\alpha$ -syn-knockout mice and also observed an absence of dopaminergic degeneration. Together, these results allowed us to conclude that both the exogenous  $\alpha$ -syn coming from the injected material and the endogenous  $\alpha$ -syn were essential to the toxicity. Building on these previous results, we are confident that the observed toxicity engages  $\alpha$ -syn both in the fraction and in the host.

We believe that our results support the notion of the existence of a range of  $\alpha$ -syn pathogenic structures with distinct toxic properties within the PD brain, in agreement with recent reports (35, 36). A recent study, using recombinant seeds, showed that among full-length, long, and short fibrils and oligomers, the short fibrils displayed the highest toxicity (28). Further work is necessary to provide a complete structural characterization of those species in patient-derived fractions, including the contribution of oligomeric species. As yet, very few studies have reported the high-resolution structures of  $\alpha$ -syn aggregates, which are, on the one hand, only derived from studies using recombinant  $\alpha$ -syn and, on the other hand, limited to near atomic resolution (37–39). Encouragingly, much effort is currently being devoted to this field of research, and three recent studies reported the atomic structure of  $\alpha$ -syn fibrils determined by cryo-electron microscopy (40–42). Unfortunately, these studies were limited to recombinant-generated  $\alpha$ -syn and not to  $\alpha$ -syn isolated from human brain tissue.

To perform a characterization of the effects of the two fractions, we developed a machine learning method to identify their biological characteristics. It is now well accepted that machine learning algorithms can be trained to detect patterns as well as, or even better

than, humans. Instead of the classification algorithms (the algorithm learns to identify in which category a sample belongs) that were mostly used in recent applications of machine learning in biology (43), we chose, in this study, to predict continuous and biologically relevant variables using MLPs. Our choice was justified by the limited sample size that is often a constraint of experimental biology. Although it might have been possible to use other feature selection methods, the use of MLPs with a distributed architecture allowed us to avoid overfitting issues and to develop a method particularly well suited for low-sample size datasets (15). As both LB- and noLB-injected monkeys displayed similar levels of degeneration, they were indistinguishable using that end point. Instead of using a clustering analysis or a classification method, hence making the a priori assumption that these groups were different, we preferred to submit the two experimental groups to the MLP independently.

The combination of this constrained, distributed architecture and the holistic approach allowed us to rank input variables according to the number of times they appeared in the group of best predictors (defined as top 1% of best networks). A major issue in the use of machine learning in experimental biology in the “black box” is the fact that it is usually impossible to “understand” how an algorithm predicts an output (44). By using a reverse engineering method, we aimed to tackle that issue. Because we explored all possible combinations of our variables, we could rank the input variables, assuming that the more they appeared in the top 1%, the more they contained information allowing precise prediction of the neurodegeneration levels. Our two experimental groups showed that some of the best predictors were similar (about 30%) but the majority was different. One could hypothesize that the variables similar between the two signatures probably embedded information related to disease progression (for example, common paths of  $\alpha$ -syn spreading once pathology is initiated), while the different ones probably contain information regarding the process of disease initiation. Further experimental studies are now needed to confirm the relevance of these variables.

In addition, as these two kinds of  $\alpha$ -syn assemblies were associated with different signatures identified by our MLP approach, we propose that our results illustrate the multifactorial nature of the disease as different mechanisms (i.e., signatures) initiated by different triggers (i.e.,  $\alpha$ -syn assemblies) led to similar consequences (i.e., degeneration levels). More important than the enrichment of a given signature for a single variable, we favor an overall interpretation, taking into consideration the multifactorial aspect of the disease.

Using this methodology, we confirmed the interest of highly expected variables but, more importantly, also unexpected variables that appear to be excellent predictors of  $\alpha$ -syn-associated dopaminergic degeneration. The first hit for LB-injected animals was phosphorylated  $\alpha$ -syn in the entorhinal cortex (as we have previously shown), followed by phosphorylated  $\alpha$ -syn in the parahippocampal cortex (unexpected), striatal microglial activation, and GABA dysregulation in the internal part of the globus pallidus (expected) (fig. S6). Conversely, Zn homeostasis was a strong predictive variable (unexpected), followed by  $\alpha$ -syn aggregation-related terms (expected) in noLB-injected animals (fig. S7).

To confirm the prediction made by the MLP approach, we first performed a retrospective literature analysis. This analysis showed that a significant part of the best predictors has been shown in the literature to be correlated with disease progression. Then, we attempted to confirm the interest of one of the top hits, the accumulation of



Zn<sup>2+</sup> in the SNpc, in independent experimental cohorts. We here describe an elevation of Zn<sup>2+</sup> levels in the SNpc of both mice injected with noLB and macaque monkeys (a different nonhuman primate subspecies than the baboons used in this study) injected with LB in striatum or SNpc. However, in mice, Zn<sup>2+</sup> dyshomeostasis was not associated with neurodegeneration in the noLB group (at odds with what was observed in monkeys), suggesting a species difference in the relationship between zinc levels and dopaminergic tract integrity. Unexpectedly, that result was not observed in rats and marmoset monkeys overexpressing human mutant  $\alpha$ -syn. This observation might suggest that Zn<sup>2+</sup> dyshomeostasis is a feature of disease not triggered in the context of human mutant  $\alpha$ -syn overexpression that is associated with fast progressing pathology (27). Then, to expand our results to human pathology, we analyzed a publicly available proteomic dataset of human samples. According to that analysis, patients with PD displayed increased levels of plasma membrane Zn<sup>2+</sup> transporters, hence suggesting a Zn dyshomeostasis in patients. In the context of PD, Zn<sup>2+</sup> dyshomeostasis has been associated with autophagy/lysosomal dysfunction in the context of *PARK9* mutations (45). Further studies are now needed to fully unravel this connection.

Together, our findings show that primate dopaminergic neurons are sensitive to both small, mostly soluble,  $\alpha$ -syn extracts and larger, aggregated,  $\alpha$ -syn extracts derived from patients with PD. These findings involve two immediate outcomes. First, soluble  $\alpha$ -syn toxicity has not been reported so far, suggesting the existence of species differences that would need to be thoroughly investigated (46) and calling for a systematic appraisal of proteinopathies in primates, particularly for validating therapeutic strategies before clinical testing (47). Second, the present study highlights the complex structure-toxicity relationship of  $\alpha$ -syn assemblies and corroborates the multifactorial origin of synucleinopathies. Distinct assemblies can induce similar degeneration (that would probably lead to similar clinical manifestation in patients) through different mechanisms, nigrostriatal or extranigral brain pathways, calling for molecular diagnosis to identify patient subpopulations before launching large-scale, heterogeneous in nature, clinical trials. Last, we developed a machine learning approach allowing quantitative assessment of the explanatory power of a given set of variables compatible with the constrained sample size of experimental biology.

## MATERIALS AND METHODS

### Access to data and machine learning code for replicability and further use by the community

The entire raw dataset is made available to the readers (table S2). Authors chose not to provide representative examples of each procedure for the sake of space and because the entire dataset is fully disclosed. Further information and requests, for examples, should be directed to and will be fulfilled by the corresponding contacts. Hyperlink to the machine learning code (<http://doi.org/10.5281/zenodo.1240558>) is provided (<https://zenodo.org/record/1240558#.XC8pqq17Su4>).

### Ethics statement

Experiments were performed in accordance with the European Union directive of 22 September 2010 (2010/63/EU) on the protection of animals used for scientific purposes. The Animal Experimentation Ethical Committee (CEEA) of the Vall d'Hebron Institute of Research approved experiments under the license number CEEA 81/13 (rats).

The Institutional Animal Care and Ethical Committee of the Bordeaux University (CE50, France) approved experiments under the license number 5012099-A (mice). The Institutional Animal Care and Ethical Committee of the Murcia University (Spain) approved experiments under the license number REGA ES300305440012 (monkeys).

## Animals and stereotactic injections

### Mice

Wild-type C57BL/6 mice (4 months old) received 2  $\mu$ l of either LB fractions or noLB fractions by stereotactic delivery to the region immediately above the right SN (coordinates from Bregma: anterior/posterior,  $-2.9$ ; lateral,  $-1.3$ ; dorsal/ventral,  $-4.5$ ) at a flow rate of 0.4  $\mu$ l/min, and the pipette was left in place for 5 min after injection to avoid leakage. Mice were euthanized 4 months after injection. Ten to 15 mice were used in each group.

### Monkeys

Animals, which were from the research animal facility of the University of Murcia (Murcia, Spain) and housed in two multi-male multi-female exterior pens, were studied in a breeding farm over 2 years (Murcia, Spain). Animals were fed fruits, vegetables, and monkey pellets twice a day before 9:00 a.m. and after 5:00 p.m. Water was available ad libitum. Seventeen healthy adult olive baboons (*Papio papio*) were used in this study. Group sizes were chosen, assuming a one-tailed  $\alpha$  of 0.05, with sample size of at least three per group, which provided >80% power to detect a difference between the treatment groups and the control group, using a Fisher's exact test. Animals were randomized into treatment or control groups. Six baboons were used for LB injections, four were used for noLB injections, and seven were untreated control animals. Intra-striatal injections of either LB or noLB fractions were performed at two rostrocaudal levels of the motor striatum (anterior commissure,  $-1$  and  $-5$  mm) under stereotactic guidance as previously described (48). The total injected volume per hemisphere was 100  $\mu$ l (two injection sites with 50  $\mu$ l each at 3  $\mu$ l/min at each location site). After each injection, the syringe was left in place for 10 min to prevent leakage along the needle track. A number of parameters were monitored during the course of the 2-year study, including survival and clinical observations. At the end of the experiment (24 months after injection), all monkeys were euthanized with pentobarbital overdose (150 mg/kg, intravenously), followed by perfusion with room temperature 0.9% saline solution (containing 1% heparin) in accordance with accepted European Veterinary Medical Association guidelines. Brains were removed quickly after death. Each brain was then dissected along the midline, and each hemisphere was divided into three parts. The left hemisphere was immediately frozen by immersion in isopentane at  $-50^{\circ}\text{C}$  for at least 5 min and stored at  $-80^{\circ}\text{C}$ . The right hemisphere was fixed for 1 week in 10 volume per tissue of 4% paraformaldehyde at  $4^{\circ}\text{C}$ , cryoprotected in two successive gradients of 20 and then 30% sucrose in phosphate-buffered saline (PBS) before being frozen by immersion in isopentane ( $-50^{\circ}\text{C}$ ) for at least 5 min, and stored at  $-80^{\circ}\text{C}$  until sectioning. Cerebrospinal fluid (CSF) and blood samples (plasma, serum, and whole blood) in the 17 animals were carefully collected before euthanasia. No samples were excluded from analysis in these studies.

### Purification of LBs from human PD brains

The samples were obtained from brains collected in a Brain Donation Program of the Brain Bank "GIE NeuroCEB" run by a consortium of Patients Associations: ARSEP (association for research on multiple



sclerosis), CSC (association for research on cerebellar ataxias), and France Alzheimer and France Parkinson. The consents were signed by the patients themselves or their next of kin in their name, in accordance with the French Bioethical Laws. The Brain Bank GIE NeuroCEB (Bioresource Research Impact Factor number BB-0033-00011) has been declared at the Ministry of Higher Education and Research and has received approval to distribute samples (agreement AC-2013-1887). Human SNpc was dissected from freshly frozen post-mortem midbrain samples from five patients with sporadic PD exhibiting conspicuous nigral LB pathology on neuropathological examination (mean age at death,  $75 \pm 2.75$  years; frozen postmortem interval,  $31.8 \pm 7.45$  hours; GIE NeuroCEB BB-0033-00011). Tissue was homogenized in 9 volumes (w/v) of ice-cold MSE buffer [10 mM Mops/KOH (pH 7.4), 1 M sucrose, 1 mM EGTA, and 1 mM EDTA] with protease inhibitor cocktail (cOMplete Mini, Boehringer Mannheim) with 12 strokes of a motor-driven glass/Teflon dounce homogenizer. For LB purification, a sucrose step gradient was prepared by overlaying 2.2 M with 1.4 M and lastly with 1.2 M sucrose in volume ratios of 3.5:8:8 (v/v). The homogenate was layered on the gradient and centrifuged at 160,000g for 3 hours using a SW 32.1 rotor (Beckman Coulter). Twenty-six fractions of 1500  $\mu$ l were collected from each gradient from top (fraction 1) to bottom (fraction 26) and analyzed for the presence of  $\alpha$ -syn aggregates by filter retardation assay, as previously described (9). Further characterization of LB fractions was performed by immunofluorescence,  $\alpha$ -syn ELISA quantification, and electron microscopy as previously described (9). For stereotactic injections, LB-containing fractions from patients with PD were mixed together in the same proportion (PD #1, fractions 19 and 20; PD #2, fractions 19 and 20; PD #3, fraction 22; PD #4, fractions 17 to 19; PD #5, fractions 20, 21, and 23). noLB-containing fractions (i.e., fraction 3, at the beginning of the 1.2 M interface) derived from the same patients with PD (which contain soluble or finely granular  $\alpha$ -syn) but lack large LB-linked  $\alpha$ -syn aggregates were obtained from the same sucrose gradient purification. Using ELISA kit against human  $\alpha$ -syn (Invitrogen, #KHB0061; following the manufacturer's recommendations),  $\alpha$ -syn concentration was measured, and both LB and noLB fractions were adjusted to  $\sim 24$  pg of  $\alpha$ -syn per microliter. In all cases, samples were bath-sonicated for 5 min before in vitro and in vivo injections.

## Characterization of noLB and LB fractions

### Electron microscopy

Briefly, carbon-coated nickel grids were covered for 1 min with corresponding fractions of interest and then washed three times with distilled water. They were then washed again in distilled water and stained for 5 min with 2% uranyl acetate before being air-dried. Digital images were obtained with a computer linked directly to a charge-coupled device camera (Gatan) on a Hitachi H-7650 electron microscope. In all cases, samples were bath-sonicated for 5 min before the in vitro applications.

### Immunofluorescence analysis of noLB and LB fractions

Indicated fractions from the sucrose gradient were spread over slides coated with poly-D-lysine and fixed with 4% paraformaldehyde in PBS for 30 min. Fixed slides were stained with 0.05% thioflavin S for 8 min and then washed three times with 80% EtOH for 5 min, followed by two washes in PBS for 5 min. Last, all samples were washed three times with PBS and blocked with 2% casein and 2% normal goat serum for 30 min. For immunofluorescence analyses, samples were incubated with human  $\alpha$ -syn-specific antibody (clone

syn211, Thermo Fisher Scientific; 1:1000) for 30 min, washed three times with PBS, and incubated with a goat anti-mouse tetramethylrhodamine (TRITC) (the Jackson laboratory; 1:500) before being coverslipped for microscopic visualization using fluorescence mounting medium.

### Dot blotting analysis

To evaluate proteinase K-resistant  $\alpha$ -syn contained in noLB and LB fractions derived from PD brains, we subjected each fraction to digestion with proteinase K (1  $\mu$ g/ml) for 0, 15, 30, 45, and 60 min. The reaction was stopped by boiling for 5 min before dot blotting with syn211 antibody. To analyze their stability, we treated noLB and LB fractions with increasing concentrations of urea (7 and 8 M) or SDS (0.5, 1, and 2%) for 6 hours at room temperature.  $\alpha$ -Syn was visualized as described above.

Filter retardation assay of noLB and LB fractions was probed with antibodies against phosphorylated  $\alpha$ -syn (Abcam, EP1536Y; 1:1000), ubiquitin (Sigma-Aldrich, U5379; 1:1000), p62 (Progen, GR62-C; 1:1000), hyperphosphorylated tau (AT8, Thermo Fisher Scientific, MN1020), or A $\beta$  (clone 6F/3D, DAKO; 1:1000).

### Human $\alpha$ -syn aggregation TR-FRET immunoassay

TR-FRET-based immunoassays were validated for total and oligomeric  $\alpha$ -syn (49). Ten microliters of noLB and LB samples were analyzed for total  $\alpha$ -syn quantification with the TR-FRET immunoassays kit against human  $\alpha$ -syn aggregation kit (Cisbio, number 6FASYPEG) according to the manufacturer's instructions.

### Velocity sedimentation and density floatation $\alpha$ -syn profiles in noLB and LB fractions

Frozen noLB and LB fraction aliquots (100  $\mu$ l) were thawed and solubilized in solubilization buffer (SB) to reach 10 mM tris (pH 7.5), 150 mM NaCl, 0.5 mM EDTA, 1 mM dithiothreitol (DTT), cOMplete EDTA-free protease inhibitors (Roche), PhosSTOP phosphatase inhibitors (Roche), benzonase (1 U/ $\mu$ l; Novagen), 2 mM MgCl<sub>2</sub>, and 2% (w/v) *N*-lauroyl-sarcosine (sarkosyl, Sigma-Aldrich) final concentrations by incubating at 37°C under constant shaking at 600 rpm (ThermoMixer, Eppendorf) for 45 min. For velocity sedimentations, a volume of 400  $\mu$ l of solubilized noLB/LB fraction was loaded on top of an 11-ml continuous 5 to 20% iodixanol gradient (OptiPrep, Sigma-Aldrich) in SB containing 0.5% (w/v) final sarkosyl concentration and linearized directly in ultracentrifuge 11-ml tubes (Seton) with a Gradient Master (Biocomp). For density floatation gradients, a volume of 400  $\mu$ l of solubilized noLB/LB fraction was mixed to reach 40% iodixanol in SB with 0.5% (w/v) final sarkosyl concentration and loaded within an 11-ml 10 to 60% discontinuous iodixanol gradient in SB with 0.5% (w/v) final sarkosyl concentration. The gradients were centrifuged at 180,000g for 3 hours (velocity) or 17 hours (density) in a swinging-bucket SW 40 Ti rotor using an Optima L-90K ultracentrifuge (Beckman Coulter). Gradients were then segregated into 16 equal fractions from the top using a piston fractionator (Biocomp) and a fraction collector (Gilson). Fractions were aliquoted for further analysis of their content by dot blot. Gradient linearity was verified by refractometry.

For dot blotting, aliquots of the collected native fractions were spotted onto Hybond polyvinylidene difluoride 0.2- $\mu$ m membranes (GE Healthcare) using a dot-blot vacuum device (Whatman). For total (MJFR1) and phosphorylated pS129 (EP1536Y)  $\alpha$ -syn immunolabeling, a step of fixation in PBS-0.1% glutaraldehyde was performed at this point, followed by three washes in PBS. Membranes were then blocked with 5% (w/v) skimmed milk powder in PBS-0.1% (v/v) Tween and probed with anti-human  $\alpha$ -syn (rabbit, Abcam, MJFR1; 1:10,000), anti-phosphorylated pS129  $\alpha$ -syn (rabbit, Abcam, EP1536Y;

1:5000), or anti- $\alpha$ -syn aggregate-specific FILA-1 (rabbit, Abcam, MJFR14-6-4-2; 1:10,000) primary antibodies in phosphate buffer saline with tween20 PBS-T-4% (w/v) bovine serum albumin (BSA) and secondary goat anti-rabbit immunoglobulin G horseradish peroxidase (HRP)-conjugated antibodies (the Jackson laboratory; 1:10,000) in phosphate buffer saline with tween20 PBS-T 1% (w/v) milk. Immunoreactivity was visualized by chemiluminescence (GE Healthcare). The amount of the respective protein in each fraction was determined by the Image Studio Lite software after acquisition of chemiluminescent signals with a ChemiDoc imager (Bio-Rad). Profiles obtained by immunoblot were normalized and plotted with SEM using the Prism software.

#### **Fourier transform infrared microspectroscopy**

One to 2  $\mu$ l of each suspension was deposited on a CaF<sub>2</sub> window and dried at room pressure and temperature. The protein aggregates were then measured in transmission at 50  $\mu$ m by 50  $\mu$ m spatial resolution with an infrared microscope (50). Depending on its size, it was possible to collect 1 to 20 spectra inside each aggregate. The infrared microscope was a Thermo Scientific Continuum equipped with a mercury cadmium telluride (MCT) detector and a 32 $\times$  0.65-numerical aperture Reflachromat objective and matching condenser, coupled to a Thermo Scientific Nicolet 8700 spectrometer with a global source and KBr beamsplitter. The microscope was operated in dual-path single-aperture mode. Spectra were recorded between 650 and 4000  $\text{cm}^{-1}$  at 2  $\text{cm}^{-1}$  resolution, with Happ-Genzel apodization and Mertz phase correction. Spectra were processed in Omnic 9.2 for automatic atmospheric correction to remove water vapor contribution.

#### **Rat ventral midbrain primary cultures**

Postnatally derived ventral midbrain cultures were prepared two steps. In the first step, rat astrocyte monolayers were generated as follows. The entire cerebral cortex from a single rat pup (postnatal days 1 and 2) was removed, diced, and then mechanically dissociated by gentle trituration. The isolated cells were plated at 80,000 cells per well under which a laminin-coated coverslip was affixed. The cells were housed at 37°C in an incubator in 5% CO<sub>2</sub> and were fed on glial media [89% minimum essential medium (MEM), 9.9% fetal calf serum, 0.33% glucose, 0.5 mM glutamine, and insulin (5  $\mu$ g/ml)]. Once confluence had been attained (about 1 week in vitro), fluorodeoxyuridine (6.7 mg/ml) and uridine (16.5 mg/ml) were added to prevent additional proliferation. In the second stage, which occurred 1 week later, rat pups aged between 1 and 2 days were anesthetized, and 1-mm<sup>3</sup> blocks containing ventral midbrain neurons were dissected from 1-mm-thick sagittal sections taken along the midline of the brain. Tissues were collected immediately into cold phosphate buffer and were treated enzymatically using papain (20 U/ml) with kynurenate (500  $\mu$ M) at 37°C under continuous oxygenation with gentle agitation for 2 hours. A dissociated cell suspension was achieved by gentle trituration and was then plated onto the pre-established glia wells at a density of 0.5 to 1.7 million neurons per well. Cultures were maintained in specially designed neuronal media [47% DMEM (Dulbecco's modified Eagle's medium), 40% Dulbecco's MEM, 10% Ham's F-12 nutrient medium, 1% calf serum, 0.25% albumin, glucose (2 mg/ml), 0.4 mM glutamine, catalase (10  $\mu$ g/ml), 50  $\mu$ M kynurenic acid, 10  $\mu$ M CNQX (6-cyano-7-nitroquinoxaline-2,3-dione), insulin (25  $\mu$ g/ml), transferrin (100  $\mu$ g/ml), superoxide dismutase (5  $\mu$ g/ml), putrescine (2.4  $\mu$ g/ml), Na<sub>2</sub>SeO<sub>3</sub> (5.2 ng/ml), triiodothyronine (0.02  $\mu$ g/ml), progesterone (62.5 ng/ml), and cortisol (40 ng/ml)] containing 27  $\mu$ M fluorodeoxy-

uridine and 68  $\mu$ M uridine to control glial outgrowth and in glial cell-derived neurotrophic factor (10 ng/ml). They were incubated for a further 7 to 8 days until the start of experiments. All TH neurons were counted on each plate following the addition of noLB and LB fractions after 1, 2, 5, and 7 days of treatment.

#### **Nonhuman primate behavioral assessment**

Following a 4-hour minimum habituation phase performed 1 day before the beginning of the observations, baboon behavior was observed outside the feeding and cleaning times, in a random order at two time points (morning and afternoon), over 4 to 9 days (eight sessions per group). On the first observational time point (i.e., 1 month after surgery), the habituation phase was performed over 3 days, allowing the observer to recognize the animals individually. We used a scan sampling method, appropriate for time budgeting (51), in which behavioral parameters were assessed every 5 min during 2-hour sessions, resulting in 192 scans per individual. Extra observational sessions were performed to avoid missing data. A unique trained observer [SC (Sandrine Camus); intraobserver reliability, Spearman rank-order correlation  $R = 0.987$ ] collected the data live on the two time points of the study: at 1 and 24 months after surgery. The observer was standing 1 m away from the outdoor cages. We focused on behavioral profiles rather than single items and used two repertoires: One reports the interaction with the environment, and one describes the position within the environment, according to published protocols (52–54). We investigated the percentages of occurrence of each item with regard to the total number of scans to obtain mean behavioral and postural time budgets, body orientation, and location profiles.

#### **Histopathological analysis**

##### **Extent of lesion**

To assess the integrity of the nigrostriatal pathway, TH immunohistochemistry was performed on SNpc and striatal sections. Briefly, 50- $\mu$ m free-floating sections from one representative level of the striatum (anterior, medial, and posterior) and serial sections (1 every 12) corresponding to the whole SNpc were incubated with a mouse monoclonal antibody raised against human TH (Millipore, MAB318; 1:5000) for one night at room temperature and revealed by an anti-mouse peroxidase EnVision System (DAKO, K400311), followed by 3,3'-diaminobenzidine (DAB) visualization. Free-floating SNpc sections were mounted on gelatinized slides, counterstained with 0.1% cresyl violet solution, dehydrated, and coverslipped, while striatal sections were mounted on gelatinized slides and coverslipped. The extent of the lesion in the striatum was quantified by optical density. Sections were scanned in an Epson Expression 10000XL high-resolution scanner, and images were used in ImageJ open-source software to compare the gray level in each region of interest, i.e., caudate nucleus and putamen. TH-positive SNpc cells were counted by stereology blind with regard to the experimental condition using a Leica DM6000 B motorized microscope coupled with the Mercator software (ExploraNova, France). The SN was delineated for each slide, and probes for stereological counting were applied to the map obtained (size of probes was 100  $\times$  80  $\mu$ m spaced by 600  $\times$  400  $\mu$ m). Each TH-positive cell with its nucleus included in the probe was counted. The optical fractionator method was lastly used to estimate the total number of TH-positive cells in the SNpc of each monkey hemisphere. In addition, we measured Nissl cell count, the volume of SN, and the surface of TH-occupied in SN to fully characterize the pattern of dopaminergic cell loss in the SN.

### ***α*-Syn pathology**

Synucleinopathy was assessed with a mouse monoclonal antibody raised against human *α*-syn (syn211) and phosphorylated *α*-syn (clone 11A5, Elan; 1:5000) immunostaining, as we previously reported (9, 27). Briefly, selected sections at two rostrocaudal levels were incubated in a same well to allow direct comparison of immunostaining intensity. Sections were incubated overnight at room temperature with the aforementioned antibodies. The following day, revelation was performed with antispecies peroxidase EnVision System (DAKO), followed by DAB incubation. Sections were then mounted on gelatinized slides, dehydrated, counterstained if necessary, and coverslipped until further analysis. Gray-level quantification or immunostaining-positive surface quantification in 40 brain regions (Fig. 2B) was performed, as previously described (27).

### **Inflammation**

Inflammatory process in the striatum, the entorhinal cortex, and the white matter of noLB- and LB-injected monkeys was measured through glial fibrillary acidic protein (GFAP)/S-100 (DAKO, Z0334/Abnova, PAP11341) and Iba1 (Abcam, ab5076) immunohistochemistry. Striatal sections of all animals were incubated together overnight with a mix of rabbit antibodies raised against GFAP and S-100 for the astroglial staining (respective dilutions, 1:2000 and 1:1000) and with a goat anti-Iba1 antibody for the microglial staining (dilution, 1:1000). These signals were revealed with antispecies peroxidase EnVision system (DAKO), followed by DAB incubation. Sections were mounted on slides, counterstained in 0.1% cresyl violet solution, dehydrated, and coverslipped. Sections stained by GFAP/S-100 were numerized at  $\times 20$  magnification with a NanoZoomer (Hamamatsu, France), and the quantification of GFAP-positive astrocytic reaction was estimated by immunostaining-positive surface quantification at regional levels with the Mercator software (ExploraNova, France). Sections stained by Iba1 were used for the microglial morphology analysis through fractal dimension quantification based on microscopic acquisitions, as previously described (55). All analyses were performed blinded to the researcher.

### **mRNA extraction and quantitative reverse transcription polymerase chain reaction**

SN samples were homogenized in TRI reagent (Euromedex, France), and RNA was isolated using a standard chloroform/isopropanol protocol. RNA was processed and analyzed following an adaptation of published methods (56). Complementary DNA (cDNA) was synthesized from 2  $\mu$ g of total RNA using RevertAid Premium Reverse Transcriptase (Fermentas) and primed with oligo-dT primers (Fermentas) and random primers (Fermentas). Quantitative polymerase chain reaction (qPCR) was performed using a LightCycler 480 Real-Time PCR System (Roche, Meylan, France). qPCRs were performed in duplicate for each sample using transcript-specific primers, cDNA (4 ng), and LightCycler 480 SYBR Green I Master (Roche) in a final volume of 10  $\mu$ l. The PCR data were exported and analyzed in an informatics tool (Gene Expression Analysis Software Environment) developed at the NeuroCentre Magendie. For the determination of the reference gene, the geNorm method was used. Relative expression analysis was corrected for PCR efficiency and normalized against two reference genes. The proteasome subunit beta type 6 (Psm6) and eukaryotic translation initiation factor 4a2 (EIF4A2) genes were used as reference genes. The relative level of expression was calculated using the comparative ( $2^{-\Delta\Delta Ct}$ ) method. Primer sequences are as follows: Psm6 (NM\_002798), CAAGAAG-

GAGGGCAGGTGTACT (forward) and CCTCCAATGGCAAAG-GACTG (reverse); EIF4a2 (NM\_001967), TGACATGGACCAGAAG-GAGAGA (forward) and TGATCAGAACACGACTTGACCCT (reverse); SNCA (CR457058), GGGCAAGAATGAA GAAGGAGC (forward) and GCCTCATTGTGACGATCCACA (reverse).

### **Biochemical analysis**

#### **Total protein extraction and quantification**

Immunoblot analyses were performed on SN, putamen, and caudate nucleus. Five tissue patches were extracted on ice using 100  $\mu$ l of radioimmunoprecipitation assay (RIPA) buffer [50 mM tris-HCl (pH 7.4), 150 mM NaCl, 1.0% Triton X-100, 0.5% Na-deoxycholate, and 0.1% SDS] with a protease inhibitor cocktail tablet (cComplete Mini, Roche Diagnostics). The lysate was placed on ice for 20 min and then centrifuged at 14,000 rpm for 15 min at 4°C. The supernatant was collected, and the bicinchoninic acid (BCA) assay was used to determine the total amount of protein in the lysates and then stored at  $-80^{\circ}\text{C}$ .

On the basis of total protein concentrations calculated from the BCA assays, aliquots of tissue lysates corresponding to known amounts of total protein per lane were prepared for each animal in Laemmli buffer [25 mM tris-HCl (pH 6.8), 7.5% glycerol, 1% SDS, 250 mM DTT, and 0.05% bromophenol blue] for immunoblotting experiment.

#### **Biochemical fractionation**

Tissue patches ( $n = 10$ ) were homogenized in 200  $\mu$ l of high-salt (HS) buffer (50 mM tris, 750 mM NaCl, 5 mM EDTA, and a cocktail of protease inhibitors and phosphatase inhibitors). Samples were sedimented at 100,000g for 20 min, and supernatants were removed for analysis. Pellets were rehomogenized in successive buffers, after which each was sedimented, and supernatant was removed: HS containing 1% Triton X-100 (HS/Triton) (variable names terminated as ultra.s1), RIPA (50 mM tris, 150 mM NaCl, 5 mM EDTA, 1% NP-40, 0.5% Na-deoxycholate, and 0.1% SDS) (variable names terminated as ultra.s12), and SDS/urea [8 M urea, 2% SDS, and 10 mM tris (pH 7.5)] (variable names terminated as ultra.p2). SDS sample buffer was added, and samples were heated to 100°C for 5 min before immunoblot analysis.

#### **Western blot analysis**

Western blots were run under all conditions from 20  $\mu$ g of protein separated by SDS-polyacrylamide gel electrophoresis and transferred to nitrocellulose. Incubation of the primary antibodies was performed overnight at 4°C with rabbit anti-LC3 (Novus Biologicals; 1:1000), rabbit anti-LAMP-2 (Santa Cruz Biotechnology; 1:1000), mouse anti-TH (Millipore; 1:1000), goat p62 (Progen; 1:1000), and mouse anti-human *α*-syn (Thermo Fisher Scientific; 1:1000). For detection of ubiquitinated proteins, proteins were transferred to polyvinylidene fluoride membranes (Millipore) and subjected to Western blot analysis using a rabbit anti-ubiquitin (Sigma-Aldrich, U5379; 1:1000). Anti-actin (Sigma-Aldrich; 1:5000) was used to control equal loading. Appropriate secondary antibodies coupled to peroxidase were revealed using a SuperSignal West Pico Chemiluminescent kit (Immobilon Western, Chemiluminescent HRP Substrate, Millipore). Chemiluminescence images were acquired using the ChemiDoc XRS+ system measurement (Bio-Rad). Signals per lane were quantified using ImageJ, and a ratio of signal on loading per animal was performed and used in statistical analyses.

#### **Dot blotting analysis of *α*-syn**

This technique was performed as we previously described (9, 34). After heating at 100°C for 5 min, 20  $\mu$ g of protein extract was diluted



in buffer (25 mM Tris-HCl, 200 mM glycine, and 1% SDS) and filtered through either a nitrocellulose membrane or an acetate cellulose membrane (Bio-Rad; 0.2- $\mu$ m pore size). Membranes were then saturated in 5% dry-skimmed milk in PBS and probed with antibodies against  $\alpha$ -syn (syn211; 1:1000), both  $\alpha$ -syn fibrils and  $\alpha$ -syn oligomers [Syn-O1; 1:10,000; (57)] (provided by O.M.A.E.-A.). Revelation was performed as described in the Western blot analysis section.

### SR-XRF microscopy elemental mapping of brain tissue cryosections

The synchrotron experiments were carried out at the Diamond Light Source, Harwell Science and Innovation Campus (Didcot, UK) with a 3-GeV energy of the storage ring and 300-mA currents with top-up injection mode. All SR-XRF microscopy investigations reported herein were carried out on the microfocus spectroscopy beamline (I18). The micro-XRF elemental mapping was acquired at room temperature with an incident x-ray energy set to 12 keV using an Si(111) monochromator and resulting in a x-ray photon flux of  $2 \times 10^{11}$  photons/s. The SN of each animal was collected from free-floating sections and mounted onto an x-ray transparent metal-free 4- $\mu$ m-thick Ultralene foil (SPEX CertiPrep, Metuchen, NJ, USA) secured to a customized polyetheretherketone holder ensuring contamination-free samples and reduced x-ray scattering contribution. The samples were affixed to a magnetic plate that connects to the sample stage. The four-element Si drift Vortex ME4 energy-dispersive detector (Hitachi High-Technologies Science America), with Xspress 3 processing electronics, was operated in the 90° geometry; hence, it minimizes the background signal. The sample-detector distance was fixed (75 mm). The sample was held at 45° to the incident x-ray beam and rastered in front of the beam, while the XRF spectra were collected. An area of 500  $\mu$ m by 500  $\mu$ m within the SNpc was mapped for each sample with a step size that matches the beam size (5  $\mu$ m) and a dwell time of 1 s per pixel due to low concentration of the element. A thin (100  $\mu$ m) pellet of the National Institute of Standards and Technology (NIST) standard reference materials SRM1577c (bovine liver material, NIST, Gaithersburg, MD, USA) was measured to calibrate experimental parameters and a thin-film XRF reference material (AXO DRESDEN GmbH). This was followed by elemental quantification through the open-source software PyMCA in which both the reference material and the sample are modeled in terms of main composition, density, and thickness. The fluorescence spectrum obtained from each pixel was fitted, the elemental concentration (micrograms per gram of dry weight or parts per million) maps were generated, and an average elemental concentration of the SNpc regions was obtained.

### Measurement of $\alpha$ -syn in monkey biological fluid samples

Multi-array 96-well plates [Meso Scale Discovery (MSD), Gaithersburg, MD, USA] were coated with 30  $\mu$ l of MJFR1 (3  $\mu$ g/ml; Abcam, Cambridge, UK) as capture antibody and incubated overnight at 4°C without shaking. The next day, plates were washed three times with 150  $\mu$ l of PBS-T [PBS (AppliChem, Darmstadt, Germany) supplemented with 0.05% Tween 20 (Roth, Karlsruhe, Germany)] per well. Unspecific binding of proteins was prevented by incubation with 150  $\mu$ l of 1% BSA (SeraCare Life Sciences, Milford, MA, USA)/PBS-T per well for 1 hour and shaking at 700 rpm. Calibrators (provided by O. El-Agnaf) were prepared from single-use aliquots of  $\alpha$ -syn (1  $\mu$ g/ml stored at  $-80^{\circ}\text{C}$  until use) and ranged from 25,000 to

6.1 pg/ml in serial fourfold dilutions. One percent of BSA/PBS-T served as blank. For the different specimen, the following dilutions were applied: 1 in 10,000 for whole blood and 1 in 8 for serum, plasma, and CSF. All dilutions were prepared in 1% BSA/PBS-T. After washing the plates, 25- $\mu$ l of the calibrator solution and diluted samples were applied to the wells and incubated as indicated above. Plates were washed again, and 25  $\mu$ l of Sulfo-TAG-labeled Syn1 antibody (BD Biosciences, Heidelberg, Germany) diluted to 1  $\mu$ g/ml in 1% PBS-T was applied to the wells as detection antibody. Sulfo-TAG labeling was performed according to the manufacturer's instruction using MSD Sulfo-TAG NHS-Ester (MSD). Incubation was done for 1 hour at 700 rpm. Plates were washed, 150  $\mu$ l of 2 $\times$  Read Buffer (MSD) was applied, and the plates were read on a MSD Sector Imager 2400. Data analysis was performed using Workbench software (MSD).

### Neurotransmitter analysis

Brain patches were dissected out on ice-cold plate, weighed, and put into 1.5-ml Eppendorf tubes. Samples were homogenized in methanol/water (50:50%, v/v) and then centrifuged at 14,000 rpm for 15 min at 4°C. The supernatant was aliquoted and stored at  $-80^{\circ}\text{C}$  until amino acid derivatization. Glutamate and GABA content in the samples was measured by high-performance liquid chromatography (HPLC) coupled with fluorometric detection (FP-2020 Plus fluorimeter, Jasco, Tokyo, Japan) after precolumn derivatization with *o*-phthaldialdehyde/mercaptoethanol (OPA) reagent. Thirty microliters of OPA reagent was automatically added to 28  $\mu$ l of sample by a refrigerated autosampler kept at 4°C (Triathlon, Spark Holland, Emmen, The Netherlands). Fifty microliters of the mixture was injected onto a 5-C18 Hypersil ODS column (3  $\times$  100 mm; Thermo Fisher Scientific, USA) perfused at 0.48 ml/min (Jasco PU-2089 Plus Quaternary Pump; Jasco, Tokyo, Japan) with a mobile phase containing 0.1 M sodium acetate, 10% methanol, and 2.2% tetrahydrofuran (pH 6.5). Chromatograms were acquired and analyzed using a ChromNAV software (Jasco, Tokyo, Japan). Under these conditions, the limits of detection for glutamate and GABA were  $\sim$ 1 and  $\sim$ 0.5 nM, and their retention times were  $\sim$ 3.5 and  $\sim$ 18.0 min, respectively.

### Multiple-layer perceptrons

Each MLP had the same architecture rule: three neurons as input, three neurons in the hidden layer, and three neurons as output. Activation function of neurons was the hyperbolic tangent. Each network was trained over 1000 presentations of a subset of the dataset. We used as error measure the mean square of differences between the expected output and the actual output. Our implementation comprises two parameters: a learning rate set at 0.05 (regulating the learning speed) and a momentum set at 0.05 (introducing purposefully a conservatism bias). Before learning, inputs were first scaled and centered (*z* scoring) to avoid dimensionality issues and then normalized between  $-0.5$  and  $0.5$ . For every combination of three variables used as inputs, 50 instances of MLP were trained with different subsets of the dataset. Eighty percent of available data have been used for learning, and the remaining 20% have been used for testing the performance of the network [elements of each subset were randomly (and uniformly) drawn for each network]. The performance from a given set of input variables was the mean of the error of the 50 instances of MLP that had data for these variables as inputs. Code was written using Python (v. 3.7.3) and the Python scientific stack: numpy (v. 1.17.2), scipy (v. 1.3.1), and Cython



(v. 0.29.13) (58). The code is fully available here (DOI: 10.5281/zenodo.1240558). Computation has been done using the Avakas cluster of the Mesocentre de Calcul Intensif Aquitaine (MCIA). RRHO test was performed as previously described (59) using RRHO package (1.14.0) in R (60) on variable list after ranking between experimental groups. Plotting was made using matplotlib (v. 3.1.1) in Python (v. 3.7.3) environment.

The association metric was based on lift calculation. Let  $a$  and  $b$  be the two variables and  $n_a$  the number of combinations including variable  $a$  and  $n$  the total number of combinations considered in the analysis. Lift calculation was then

$$\text{Lift}_{ab} = \frac{n_{ab}/n_b}{n_a/n}$$

The lift calculation was then corrected for performance to avoid selection of detrimental association by being divided by the mean prediction error of the duo.

### Quantification and statistical analysis

Regarding the data analysis for Fourier transform infrared microscopy, spectra were analyzed by PCA. PCA is a multivariate statistical analysis technique that captures independent sources of variance in the data and represents them in principal components (eigenvectors) that carry the underlying spectral information and in a score plot that shows the relation between spectra and can be used to cluster the data based on the spectral information. PCA was performed in The Unscrambler X 10.3 (CAMO Software) using the singular value decomposition algorithm with leverage correction. Two series of preprocessing were applied before PCA and compared. Spectra were either baseline-corrected in the amide I region between 1590 and 1700  $\text{cm}^{-1}$  and vector-normalized or their second derivatives were computed and vector-normalized.

Statistical analyses were performed with GraphPad Prism 6.0 (GraphPad Software Inc., San Diego, CA). For all experiments, comparisons among means were performed using one-way analysis of variance (ANOVA), followed, if appropriate, by a pairwise comparison between means by Tukey post hoc analysis. All values are expressed as the means  $\pm$  SEM. Size effect was assessed with Cohen's  $d$  analysis. In all analyses, statistical significance was set at  $P < 0.05$ .

### SUPPLEMENTARY MATERIALS

Supplementary material for this article is available at <http://advances.sciencemag.org/cgi/content/full/6/20/eaaz9165/DC1>

[View/request a protocol for this paper from Bio-protocol.](#)

### REFERENCES AND NOTES

- H. Braak, K. Del Tredici, U. Rüb, R. A. I. de Vos, E. N. H. Jansen Steur, E. Braak, Staging of brain pathology related to sporadic Parkinson's disease. *Neurobiol. Aging* **24**, 197–211 (2003).
- J. H. Kordower, Y. Chu, R. A. Hauser, T. B. Freeman, C. W. Olanow, Lewy body-like pathology in long-term embryonic nigral transplants in Parkinson's disease. *Nat. Med.* **14**, 504–506 (2008).
- J. Y. Li, E. Englund, J. L. Holton, D. Soulet, P. Hagell, A. J. Lees, T. Lashley, N. P. Quinn, S. Rehncrona, A. Björklund, H. Widner, T. Revesz, O. Lindvall, P. Brundin, Lewy bodies in grafted neurons in subjects with Parkinson's disease suggest host-to-graft disease propagation. *Nat. Med.* **14**, 501–503 (2008).
- I. Mendez, A. Viñuela, A. Astradsson, K. Mukhida, P. Hallett, H. Robertson, T. Tierney, R. Holness, A. Dagher, J. Q. Trojanowski, O. Isacson, Dopamine neurons implanted into people with Parkinson's disease survive without pathology for 14 years. *Nat. Med.* **14**, 507–509 (2008).
- B. Dehay, M. Vila, E. Bezdard, P. Brundin, J. H. Kordower, Alpha-synuclein propagation: New insights from animal models. *Mov. Disord.* **31**, 161–168 (2016).
- B. Winner, R. Jappelli, S. K. Maji, P. A. Desplats, L. Boyer, S. Aigner, C. Hetzer, T. Loher, M. Vilar, S. Campioni, C. Tzitzilonis, A. Soragni, S. Jessberger, H. Mira, A. Consiglio, E. Pham, E. Masliah, F. H. Gage, R. Riek, In vivo demonstration that  $\alpha$ -synuclein oligomers are toxic. *Proc. Natl. Acad. Sci. U.S.A.* **108**, 4194–4199 (2011).
- N. Bengoa-Vergniory, R. F. Roberts, R. Wade-Martins, J. Alegre-Abarrategui, Alpha-synuclein oligomers: A new hope. *Acta Neuropathol.* **134**, 819–838 (2017).
- Y. Chu, S. Muller, A. Tavares, O. Barret, D. Alagille, J. Seibyl, G. Tamagnan, K. Marek, K. C. Luk, J. Q. Trojanowski, V. M. Y. Lee, J. H. Kordower, Intrastriatal alpha-synuclein fibrils in monkeys: Spreading, imaging and neuropathological changes. *Brain* **142**, 3565–3579 (2019).
- A. Recasens, B. Dehay, J. Bové, I. Carballo-Carbajal, S. Dovero, A. Pérez-Villalba, P.-O. Fernagut, J. Blesa, A. Parent, C. Perier, I. Fariñas, J. A. Obeso, E. Bezdard, M. Vila, Lewy body extracts from Parkinson disease brains trigger  $\alpha$ -synuclein pathology and neurodegeneration in mice and monkeys. *Ann. Neurol.* **75**, 351–362 (2014).
- K. C. Luk, V. Kehm, J. Carroll, B. Zhang, P. O'Brien, J. Q. Trojanowski, V. M. Y. Lee, Pathological  $\alpha$ -synuclein transmission initiates Parkinson-like neurodegeneration in nontransgenic mice. *Science* **338**, 949–953 (2012).
- W. Peelaerts, L. Bousset, A. Van der Perren, A. Moskaluk, R. Pulizzi, M. Giugliano, C. Van den Haute, R. Melki, V. Baekelandt,  $\alpha$ -Synuclein strains cause distinct synucleinopathies after local and systemic administration. *Nature* **522**, 340–344 (2015).
- E. Bezdard, S. Dovero, C. Prunier, P. Ravenscroft, S. Chalou, D. Guilloteau, A. R. Crossman, B. Bioulac, J. M. Brotchie, C. E. Gross, Relationship between the appearance of symptoms and the level of nigrostriatal degeneration in a progressive 1-methyl-4-phenyl-1,2,3,6-tetrahydropyridine-lesioned macaque model of Parkinson's disease. *J. Neurosci.* **21**, 6853–6861 (2001).
- M. Bourdenx, A. Nioche. (2018).
- K. Hornik, M. Stinchcombe, H. White, Multilayer feedforward networks are universal approximators. *Neural Netw.* **2**, 359–366 (1989).
- L. I. Kuncheva, J. J. Rodríguez, On feature selection protocols for very low-sample-size data. *Pattern Recognit.* **81**, 660–673 (2018).
- R. L. Albin, A. B. Young, J. B. Penney, The functional anatomy of basal ganglia disorders. *Trends Neurosci.* **12**, 366–375 (1989).
- M. Neumann, V. Müller, H. A. Kretzschmar, C. Haass, P. J. Kahle, Regional distribution of proteinase K-resistant  $\alpha$ -synuclein correlates with Lewy body disease stage. *J. Neuropathol. Exp. Neurol.* **63**, 1225–1235 (2004).
- E. Kövari, G. Gold, F. R. Herrmann, A. Canuto, P. R. Hof, C. Bouras, P. Giannakopoulos, Lewy body densities in the entorhinal and anterior cingulate cortex predict cognitive deficits in Parkinson's disease. *Acta Neuropathol.* **106**, 83–88 (2003).
- L. Silveira-Moriyama, J. L. Holton, A. Kingsbury, H. Ayling, A. Petrie, W. Sterlacci, W. Poewe, H. Maier, A. J. Lees, T. Revesz, Regional differences in the severity of Lewy body pathology across the olfactory cortex. *Neurosci. Lett.* **453**, 77–80 (2009).
- Y. C. Wong, D. Krainic,  $\alpha$ -synuclein toxicity in neurodegeneration: Mechanism and therapeutic strategies. *Nat Med* **23**, 1–13 (2017).
- B. Dehay, J. Bové, N. Rodríguez-Muela, C. Perier, A. Recasens, P. Boya, M. Vila, Pathogenic lysosomal depletion in Parkinson's disease. *J. Neurosci.* **30**, 12535–12544 (2010).
- S. Kaushik, A. M. Cuervo, Proteostasis and aging. *Nat. Med.* **21**, 1406–1415 (2015).
- E. C. Hirsch, S. Vyas, S. Hunot, Neuroinflammation in Parkinson's disease. *Parkinsonism Relat. Disord.* **18**, S210–S212 (2012).
- D. T. Dexter, A. Carayon, F. Javoy-Agid, Y. Agid, F. R. Wells, S. E. Daniel, A. J. Lees, P. Jenner, C. D. Marsden, Alterations in the levels of iron, ferritin and other trace metals in Parkinson's disease and other neurodegenerative diseases affecting the basal ganglia. *Brain* **114**, 1953–1975 (1991).
- K. Du, M.-Y. Liu, X. Zhong, M.-J. Wei, Decreased circulating zinc levels in Parkinson's disease: A meta-analysis study. *Sci. Rep.* **7**, 3902 (2017).
- J.-Y. Lee, H. J. Son, J. H. Choi, E. Cho, J. Kim, S. J. Chung, O. Hwang, J.-Y. Koh, Cytosolic labile zinc accumulation in degenerating dopaminergic neurons of mouse brain after MPTP treatment. *Brain Res.* **1286**, 208–214 (2009).
- M. Bourdenx, S. Dovero, M. Engeln, S. Bido, M. F. Bastide, N. Duthel, I. Vollenweider, L. Baud, C. Piron, V. Grouthier, T. Boraud, G. Porras, Q. Li, V. Baekelandt, D. Scheller, A. Michel, P.-O. Fernagut, F. Georges, G. Courtine, E. Bezdard, B. Dehay, Lack of additive role of ageing in nigrostriatal neurodegeneration triggered by  $\alpha$ -synuclein overexpression. *Acta Neuropathol. Commun.* **3**, 46 (2015).
- J. M. Froula, M. Castellana-Cruz, N. M. Anabtawi, J. D. Camino, S. W. Chen, D. R. Thrasher, J. Freire, A. A. Yazdi, S. Fleming, C. M. Dobson, J. R. Kumita, N. Cremades, L. A. Volpicelli-Daley, Defining  $\alpha$ -synuclein species responsible for Parkinson's disease phenotypes in mice. *J. Biol. Chem.* **294**, 10392–10406 (2019).

29. G. Piatetsky-Shapiro, in *Knowledge Discovery in Databases*, G. Piatetsky-Shapiro, W. J. Frawley, Eds. (AAAI/MIT Press, 1991).
30. J. P. Bolam, E. K. Pissadaki, Living on the edge with too many mouths to feed: Why dopamine neurons die. *Mov. Disord.* **27**, 1478–1483 (2012).
31. D. J. Surmeier, J. A. Obeso, G. M. Halliday, Selective neuronal vulnerability in Parkinson disease. *Nat. Rev. Neurosci.* **18**, 101–113 (2017).
32. I. Carballo-Carbajal, A. Laguna, J. Romero-Giménez, T. Cuadros, J. Bové, M. Martínez-Vicente, A. Parent, M. Gonzalez-Sepulveda, N. Peñuelas, A. Torra, B. Rodríguez-Galván, A. Ballabio, T. Hasegawa, A. Bortolozzi, E. Gelpi, M. Vila, Brain tyrosinase overexpression implicates age-dependent neuromelanin production in Parkinson's disease pathogenesis. *Nat. Commun.* **10**, 973 (2019).
33. M. E. Johnson, B. Stecher, V. Labrie, L. Brundin, P. Brundin, Triggers, facilitators, and aggravators: Redefining Parkinson's disease pathogenesis. *Trends Neurosci.* **42**, 4–13 (2019).
34. M. Bourdenx, N. S. Koulakiotis, D. Sanoudou, E. Bezdard, B. Dehay, A. Tsaropoulos, Protein aggregation and neurodegeneration in prototypical neurodegenerative diseases: Examples of amyloidopathies, tauopathies and synucleinopathies. *Prog. Neurobiol.* **155**, 171–193 (2017).
35. A. Lau, R. W. L. So, H. H. C. Lau, J. C. Sang, A. Ruiz-Riquelme, S. C. Fleck, E. Stuart, S. Menon, N. P. Visanji, G. Meisl, R. Faidi, M. M. Marano, C. Schmitt-Ulms, Z. Wang, P. E. Fraser, A. Tandon, B. T. Hyman, H. Wille, M. Ingelsson, D. Klenerman, J. C. Watts,  $\alpha$ -Synuclein strains target distinct brain regions and cell types. *Nat. Neurosci.* **23**, 21–31 (2019).
36. T. Strohäker, B. C. Jung, S.-H. Liou, C. O. Fernandez, D. Riedel, S. Becker, G. M. Halliday, M. Bennati, W. S. Kim, S.-J. Lee, M. Zweckstetter, Structural heterogeneity of  $\alpha$ -synuclein fibrils amplified from patient brain extracts. *Nat. Commun.* **10**, 5535 (2019).
37. J. A. Rodriguez, M. I. Ivanova, M. R. Sawaya, D. Cascio, F. E. Reyes, D. Shi, S. Sangwan, E. L. Guenther, L. M. Johnson, M. Zhang, L. Jiang, M. A. Arbing, B. L. Nannenga, J. Hattne, J. Whitelegge, A. S. Brewster, M. Messerschmidt, S. Boutet, N. K. Sauter, T. Gonen, D. S. Eisenberg, Structure of the toxic core of  $\alpha$ -synuclein from invisible crystals. *Nature* **525**, 486–490 (2015).
38. M. D. Tuttle, G. Comellas, A. J. Nieuwkoop, D. J. Covell, D. A. Berthold, K. D. Kloepper, J. M. Courtney, J. K. Kim, A. M. Barclay, A. Kendall, W. Wan, G. Stubbs, C. D. Schwieters, V. M. Y. Lee, J. M. George, C. M. Rienstra, Solid-state NMR structure of a pathogenic fibril of full-length human  $\alpha$ -synuclein. *Nat. Struct. Mol. Biol.* **23**, 409–415 (2016).
39. L. Bousset, L. Pieri, G. Ruiz-Arlandis, J. Gath, P. H. Jensen, B. Habenstein, K. Madiona, V. Olieric, A. Böckmann, B. H. Meier, R. Melki, Structural and functional characterization of two  $\alpha$ -synuclein strains. *Nat. Commun.* **4**, 2575 (2013).
40. Y. Li, C. Zhao, F. Luo, Z. Liu, X. Gui, Z. Luo, X. Zhang, D. Li, C. Liu, X. Li, Amyloid fibril structure of  $\alpha$ -synuclein determined by cryo-electron microscopy. *Cell Res.* **28**, 897–903 (2018).
41. R. Guerrero-Ferreira, N. M. Taylor, D. Mona, P. Ringler, M. E. Lauer, R. Riek, M. Britschgi, H. Stahlberg, Cryo-EM structure of alpha-synuclein fibrils. *eLife* **7**, e36402 (2018).
42. D. R. Boyer, B. Li, C. Sun, W. Fan, M. R. Sawaya, L. Jiang, D. S. Eisenberg, Structures of fibrils formed by  $\alpha$ -synuclein hereditary disease mutant H50Q reveal new polymorphs. *Nat. Struct. Mol. Biol.* **26**, 1044–1052 (2019).
43. A. Esteva, B. Kuprel, R. A. Novoa, J. Ko, S. M. Swetter, H. M. Blau, S. Thrun, Dermatologist-level classification of skin cancer with deep neural networks. *Nature* **542**, 115–118 (2017).
44. D. Castelvecchi, Can we open the black box of AI? *Nature* **538**, 20–23 (2016).
45. J.-S. Park, B. Koentjoro, D. Veivers, A. Mackay-Sim, C. M. Sue, Parkinson's disease-associated human ATP13A2 (PARK9) deficiency causes zinc dyshomeostasis and mitochondrial dysfunction. *Hum. Mol. Genet.* **23**, 2802–2815 (2014).
46. E. Diguët, C. E. Gross, F. Tison, E. Bezdard, Rise and fall of minocycline in neuroprotection: Need to promote publication of negative results. *Exp. Neurol.* **189**, 1–4 (2004).
47. R. Aron Badin, M. Vadori, E. Cozzi, P. Hantraye, Translational research for Parkinson's disease: The value of pre-clinical primate models. *Eur. J. Pharmacol.* **759**, 118–126 (2015).
48. M. Ahmed, A. Berthet, E. Bychkov, G. Porras, Q. Li, B. H. Bioulac, Y. T. Carl, B. Bloch, S. Kook, I. Aubert, S. Dovero, E. Doudnikoff, V. V. Gurevich, E. V. Gurevich, E. Bezdard, Lentiviral overexpression of GRK6 alleviates L-dopa-induced dyskinesia in experimental Parkinson's disease. *Sci. Transl. Med.* **2**, 28ra28 (2010).
49. M. Bidinosti, D. R. Shimshek, B. Mollenhauer, D. Marcellin, T. Schweizer, G. P. Lotz, M. G. Schlossmacher, A. Weiss, Novel one-step immunoassays to quantify  $\alpha$ -Synuclein: Applications for biomarker development and high-throughput screening. *J. Biol. Chem.* **287**, 33691–33705 (2012).
50. G. Zandomenighi, M. R. H. Krebs, M. G. McCammon, M. Fändrich, FTIR reveals structural differences between native  $\beta$ -sheet proteins and amyloid fibrils. *Protein Sci.* **13**, 3314–3321 (2004).
51. J. Altmann, Observational study of behavior: Sampling methods. *Behaviour* **49**, 227–267 (1974).
52. S. M. J. Camus, C. Blois-Heulin, Q. Li, M. Hausberger, E. Bezdard, Behavioural profiles in captive-bred cynomolgus macaques: Towards monkey models of mental disorders? *PLOS ONE* **8**, e62141 (2013).
53. S. M. Camus, C. Rochais, C. Blois-Heulin, Q. Li, M. Hausberger, E. Bezdard, Birth origin differentially affects depressive-like behaviours: Are captive-born cynomolgus monkeys more vulnerable to depression than their wild-born counterparts? *PLOS ONE* **8**, e67711 (2013).
54. S. M. J. Camus, C. Rochais, C. Blois-Heulin, Q. Li, M. Hausberger, E. Bezdard, Depressive-like behavioral profiles in captive-bred single- and socially-housed rhesus and cynomolgus macaques: A species comparison. *Front. Behav. Neurosci.* **8**, 47 (2014).
55. F. N. Soria, M. Engelm, M. Martínez-Vicente, C. Glangetas, M. J. López-González, S. Dovero, B. Dehay, E. Normand, M. Vila, A. Favereaux, F. Georges, C. L. Bianco, E. Bezdard, P.-O. Fernagut, Glucocerebrosidase deficiency in dopaminergic neurons induces microglial activation without neurodegeneration. *Hum. Mol. Genet.* **26**, 2603–2615 (2017).
56. S. A. Bustin, V. Benes, J. A. Garson, J. Hellemans, J. Huggett, M. Kubista, R. Mueller, T. Nolan, M. W. Pfaffl, G. L. Shipley, J. Vandesompele, C. T. Wittwer, The MIQE guidelines: Minimum information for publication of quantitative real-time PCR experiments. *Clin. Chem.* **55**, 611–622 (2009).
57. N. N. Vaikath, N. K. Majbour, K. E. Paleologou, M. T. Ardah, E. van Dam, W. D. J. van de Berg, S. L. Forrest, L. Parkkinen, W.-P. Gai, N. Hattori, M. Takanashi, S.-J. Lee, D. M. A. Mann, Y. Imai, G. M. Halliday, J.-Y. Li, O. M. A. el-Agnaf, Generation and characterization of novel conformation-specific monoclonal antibodies for  $\alpha$ -synuclein pathology. *Neurobiol. Dis.* **79**, 81–99 (2015).
58. P. Virtanen, R. Gommers, T. E. Oliphant, M. Haberland, T. Reddy, D. Cournapeau, E. Burovski, P. Peterson, W. Weckesser, J. Bright, S. J. van der Walt, M. Brett, J. Wilson, K. Jarrod Millman, N. Mayorov, A. R. J. Nelson, E. Jones, R. Kern, E. Larson, C. J. Carey, Í. Polat, Y. Feng, E. W. Moore, J. V. Plas, D. Laxalde, J. Perktold, R. Cimrman, I. Henriksen, E. A. Quintero, C. R. Harris, A. M. Archibald, A. H. Ribeiro, F. Pedregosa, P. van Mulbregt, SciPy 1.0 Contributors, SciPy 1.0—Fundamental algorithms for scientific computing in Python. arXiv:1907.10121 [cs.LG] (23 July 2019).
59. S. B. Plaisier, R. Taschereau, J. A. Wong, T. G. Graeber, Rank-rank hypergeometric overlap: Identification of statistically significant overlap between gene-expression signatures. *Nucleic Acids Res.* **38**, e169 (2010).
60. R. C. Team, *R: A Language and Environment for Statistical Computing* (R Foundation for Statistical Computing, 2016).

**Acknowledgments:** We wish to express our gratitude to A. R. Crossman (University of Manchester, UK) for comments for language supervision. We also thank M. Bosc (Cold Spring Harbor, USA) for valuable comments on the manuscript. We thank C. L. Martínez (Veterinary Service, University of Murcia) for administrative assistance; M. F. Ros Romero and J. Martínez Rabadán (University of Murcia) for veterinary and husbandry support; A. L. Gil, L. Cuenca, and I. Mascarell from the Clinical and Experimental Neuroscience group (University of Murcia) for technical help with various parts of the in vivo part of these complex experiments. We would like to thank P. Hantraye (MIRcen) for providing baboon stereotaxic frame. The University of Bordeaux and the CNRS provided infrastructural support. **Funding:** This work was supported by a grant from the Michael J. Fox Foundation (project grant number 2013-8499), Fundación de Investigación HM Hospitales (Madrid, Spain), the Fundación Séneca (project grant number F519540/PI/14), the TARGET PD ANR grant, and The Simone and Cino Del Duca Prize from the French Academy of Sciences. J.-A.O. and I.T.D. were funded by MINECO/AEI/FEDER-UE (SAF2015-67239-P). M.B. and M.-L.A. were supported by a Ministère de l'Enseignement Supérieur et de la Recherche fellowship and the France Parkinson Foundation (M.B.). The help of the Bordeaux Imaging Center, part of the national infrastructure France Biomed, granted by ANR-10INBS-04-0, is acknowledged. The human  $\alpha$ -Syn aggregation TR-FRET immunoassay was performed in the Biochemistry and Biophysics Platform of the Bordeaux Neurocampus at the Bordeaux University funded by the LABEX BRAIN (ANR-10-LABX-43) with the help of Y. Rufin. Computing time for this study was provided by the MClA, the public research HPC center in Aquitaine, France. The samples were obtained from the Brain Bank GIE NeuroCEB (BRIF number 0033-00011), funded by the patients' associations France Alzheimer, France Parkinson, ARSEP, and "Connaître les Syndromes Cérébelleux" to which we express our gratitude. The synchrotron Diamond is acknowledged for provision of beam time (exp. SP13009). **Author contributions:** M.B., M.V., J.A.O., P.D., B.D., and E.B. conceived and designed the study. M.B., G.P., I.T.D., C.E., N.G.-C., M.T.H., B.D., and E.B. performed the surgeries. S.C. and C.E. performed the behavioral analyses. M.G. set up the actimetry behavioral platform. S.D., M.-L.A., A.P., and P.A. performed the histologic and immunohistochemical analysis of the data. S.D., A.P., and M.-L.A. performed the imaging experiments. E.D. performed the electron microscopy analysis. F.L., M.-L.A., and M.-L.T. performed the biochemistry experiments. C.P. performed and analyzed the primary culture experiment. M.-L.A., S.B., and B.D. performed the synchrotron analysis. C.S. performed the infrared microscopy. N.K. and B.M.

performed biological fluid analysis. S.N. and M.M. performed the HPLC analysis. T.L.-L. performed the mRNA extraction and qPCR analysis. M.B., A.N., S.D., M.-L.A., S.C., N.P.R., S.B., C.S., F.L., N.K., B.M., S.N., M.M., C.P., A.R., N.N.V., O.M.A.E.-A., M.T.H., P.D., M.V., J.A.O., B.D., and E.B. analyzed the data. M.B., A.N., and N.P.R. developed the MLP approach. M.B., M.V., J.A.O., B.D., and E.B. wrote the paper. M.T.H. supervised the in vivo phase of the experiments, while B.D. and E.B. supervised the whole project. All authors discussed the results, assisted in the preparation, and contributed to the manuscript. All authors approved the final version of the manuscript. **Competing interests:** E.B. is a director and a shareholder of the Motac Neuroscience Ltd. The other authors declare that they have no competing interests. **Data and materials availability:** The entire raw dataset is made available to the readers (table S2). The authors chose not to provide representative examples of each procedure for the sake of space and because the entire dataset is fully disclosed. Further information and requests for examples should be directed to and will be fulfilled by the corresponding contacts. Hyperlink to the machine learning code

(<http://doi.org/10.5281/zenodo.1240558>) is provided (<https://zenodo.org/record/1240558#.XC8pqy17Su4>).

Submitted 21 October 2019

Accepted 6 March 2020

Published 13 May 2020

10.1126/sciadv.aaz9165

**Citation:** M. Bourdenx, A. Nioche, S. Dovero, M.-L. Arotcarena, S. Camus, G. Porras, M.-L. Thiolat, N. P. Rougier, A. Prigent, P. Aubert, S. Bohic, C. Sandt, F. Laferrière, E. Doudnikoff, N. Kruse, B. Mollenhauer, S. Novello, M. Morari, T. Leste-Lasserre, I. T. Damas, M. Goillandeau, C. Perier, C. Estrada, N. Garcia-Carrillo, A. Recasens, N. N. Vaikath, O. M. A. El-Agnaf, M. T. Herrero, P. Derkinderen, M. Vila, J. A. Obeso, B. Dehay, E. Bezard, Identification of distinct pathological signatures induced by patient-derived  $\alpha$ -synuclein structures in nonhuman primates. *Sci. Adv.* **6**, eaaz9165 (2020).